9th International Scientific Colloquium

MMP

Modelling for Materials Processing

Rīga, September 18-19, 2023

MMP2023 Poster session
September 18. 2023

UNIVERSITY OF LATVIA

Leibniz Universität Hannover

Organized by

Institute of Numerical Modelling

INSTITUTE OF PHYSICS

UNIVERSITY OF LATVIA FACULTY OF PHYSICS, MATHEMATICS AND OPTOMETRY

Modelling for Materials Processing
Rīga, September 2023

UNIVERSITY OF LATVIA · Leibniz Universität Hannover · University of Latvia Institute of Physics

Magnetic field distribution in disc-type electromagnetic pump with permanent magnets

Arturs Brekis[1, 2]*, Andrey Shishko[1], Imants Bucenieks[1]
[1] University of Latvia, Jelgavas street 3, Riga LV-1004, Latvia *arturs.brekis@lu.lv
[2] Riga Technical University, Azenes street 8, Riga LV-1006, Latvia

Introduction

The electromagnetic pumps on permanent magnets are a promising technology for liquid metal transportation using magnetohydrodynamic interaction between electrically conducting fluid and magnetic field. In this article, a permanent magnet disc-type Na electromagnetic pump magnetic field is studied.

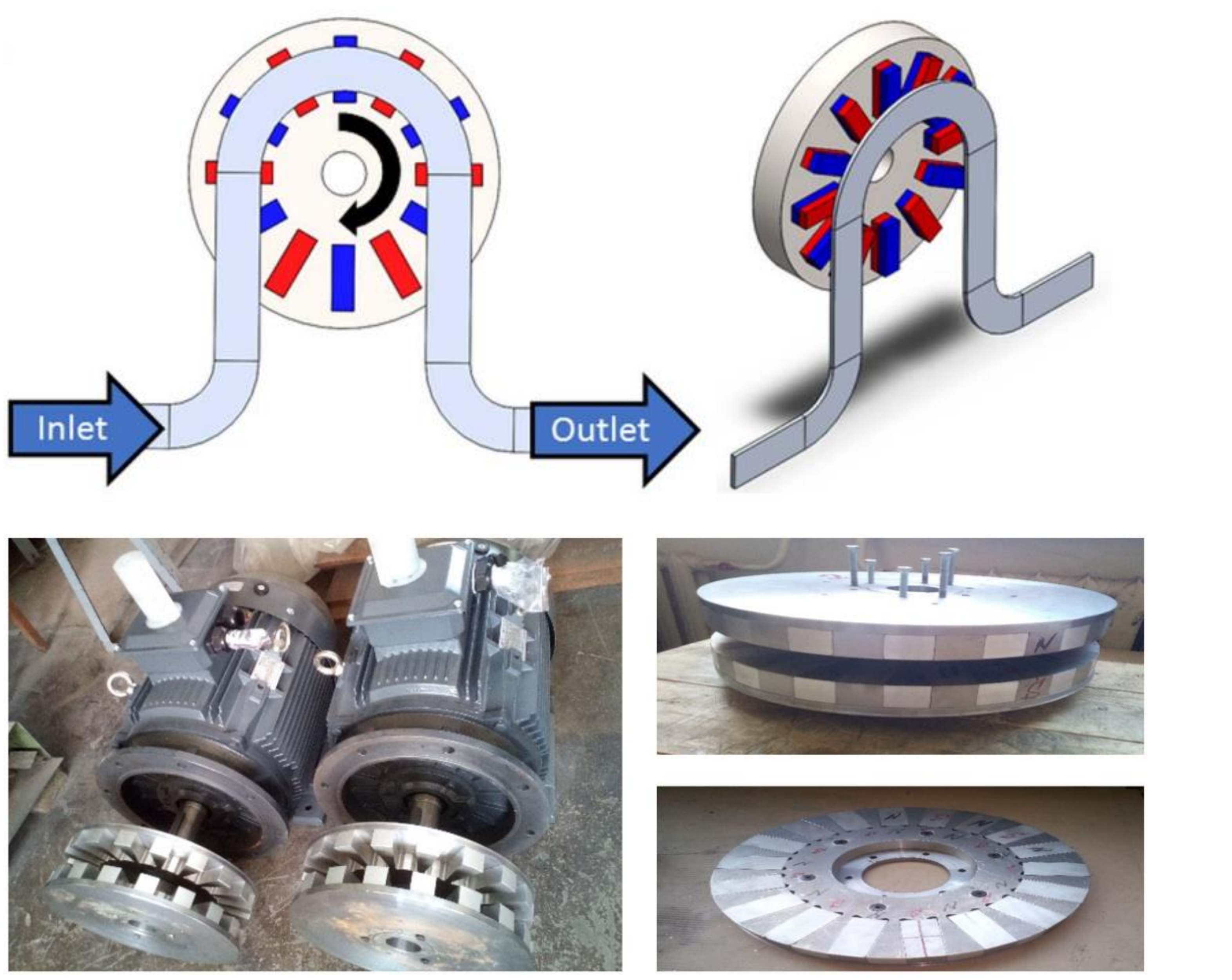

Fig. 1. *Permanent magnet disc-type magnetohydrodynamic pump principle (upper) [1]. Two pumps (lower left) in the manufacturing stage; one fully assembled magnet system (lower- top right); one assembled set of permanent magnets on a disc (bottom right).*

Field measurements and simulation

Numerical 3D field distribution is provided and compared with experimentally measured magnetic field mapping in the liquid metal channel.

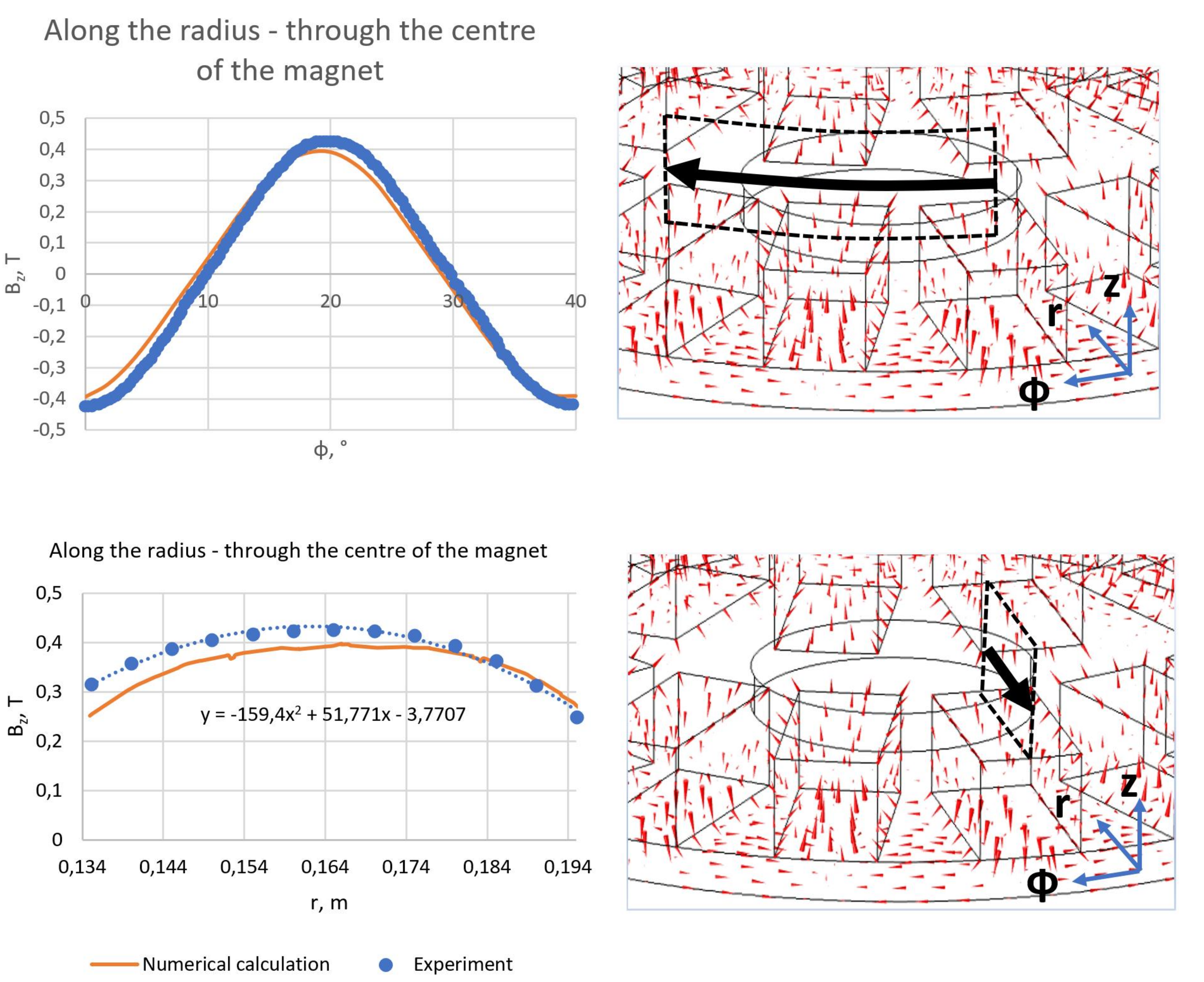

Fig. 2. *Experimentally measured field distribution along the radius (upper) and azimuth (lower) together with its comparison with numerical simulation (left); spatial distribution of the magnetic field (right).*

Pressure – flowrate characteristic curves of the pump

Using an electrodynamic approach, the magnetic field data is further used to calculate the pump p-Q characteristics in the solid body approximation:

$$\langle j_r \rangle = \frac{1}{1+\varkappa}\left\{\frac{1}{\rho}\frac{\partial \Psi}{\partial \varphi} + \sigma \varkappa V_{\varphi} \langle B_z \rangle\right\}$$

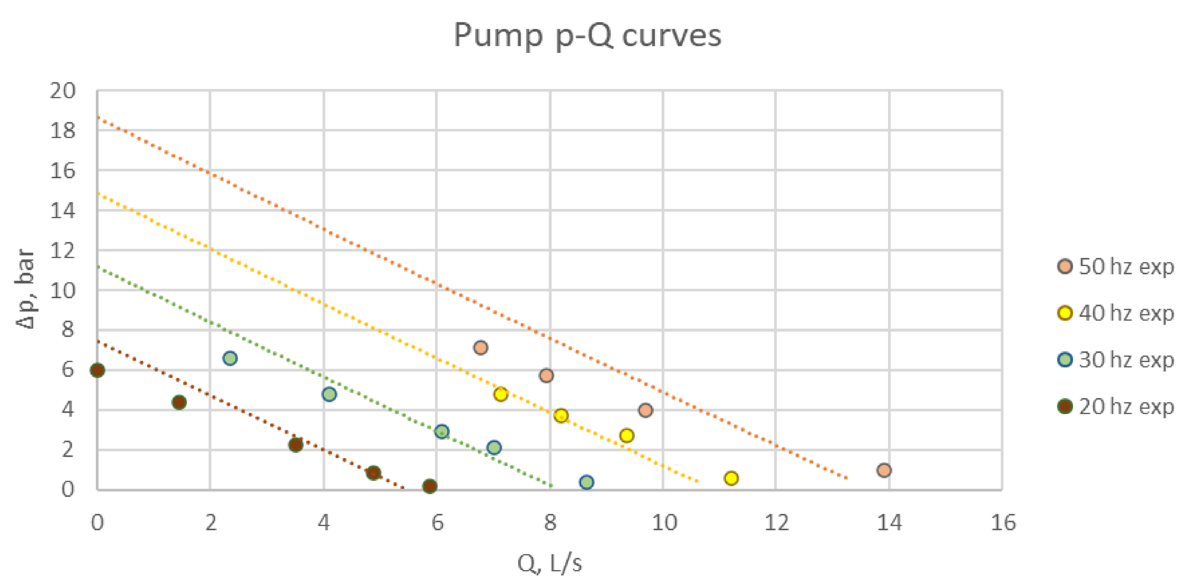

Fig. 3. *Experimental pressure-flowrate curves of the pump and their comparison with theoretical ones.*

A good agreement is obtained with experimentally measured p-Q characteristics during the pump prototype tests. The experiment was conducted on the newly designed 150-200°C liquid sodium loop at the Institute of Physics of the University of Latvia (IPUL).

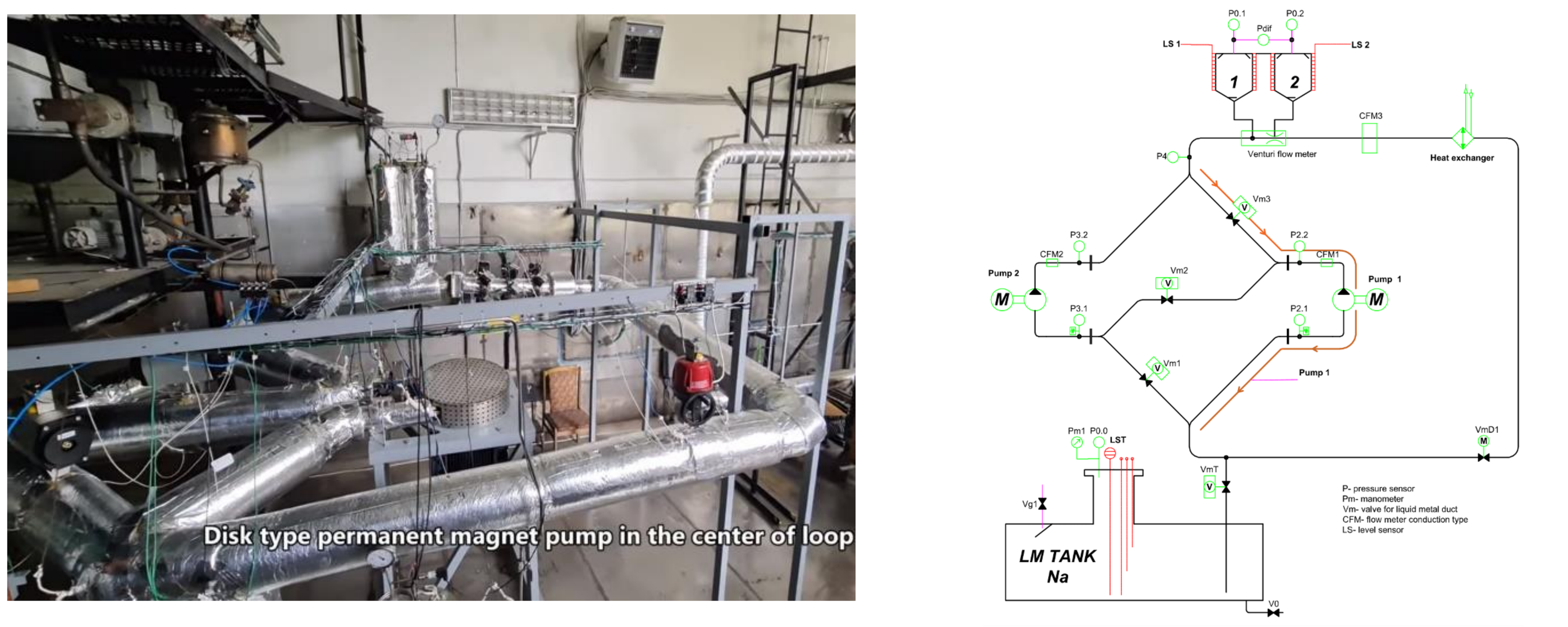

Fig. 4. *The used experimental sodium loop; photo (left); scheme (right) [2].*

References and acknowledgements

[1] M.G. Hvasta, W.K. Nollet, M.H. Anderson, "Designing moving magnet pumps for high-temperature, liquid-metal systems", Nuclear Engineering and Design, Vol. 327, 2018, p. 228-237.
[2] A. Brekis, L. Buligins, I. Bucenieks, K. Kravalis, A. Lacis, O. Mikanovskis. "MHD pump with rotating permanent magnets: inlet pressure influence on p-Q curves", Magnetohydrodynamics. Vol. 58, 2022, p. 475-482.

The research was supported by European project of the Institute of Physics of the University of Latvia, no. KC-PI-2017/3 "Commercialization of Cascadable Electromagnetic Pumps with Permanent Magnets with Stabilized Parameters"

Conclusions

Pump experiments on the Na loop showed that the obtained p-Q curves agree well with the theory. This shows that when applying the solid body approximation without taking into account hydrodynamic aspects, in this case, it is possible to obtain reliable performance curves using the knowledge of the magnetic field distribution, which can be obtained numerically or experimentally.

Modelling for Materials Processing
Riga, September 2023

UNIVERSITY OF LATVIA

Leibniz Universität Hannover

Numerical analysis of condensation risk in different multilayer building structures

B. Jirgensone, A. Jakovics
Institute of Numerical Modelling, University of Latvia, Jelgavas street 3, Riga LV-1004, Latvia

Introduction

In this numerical study we compare thermal comfort conditions in different structures with cooling conditions in capillary heating systems and will it affect mold risk in the constructions. Numerical models were created in WuFi and Comsol. Both programs model one-dimensional and use the finite volume method. Each structure was adapted to the walls, ceilings and floors in the experiment. The properties of the construction materials have been searched from the available resources and compared as much as possible to the existing materials. In order to have as similar boundary conditions as possible in both programs, calculations be performed initially without moisture and heat radiation transfer, and after moisture and heat radiation will be applied.

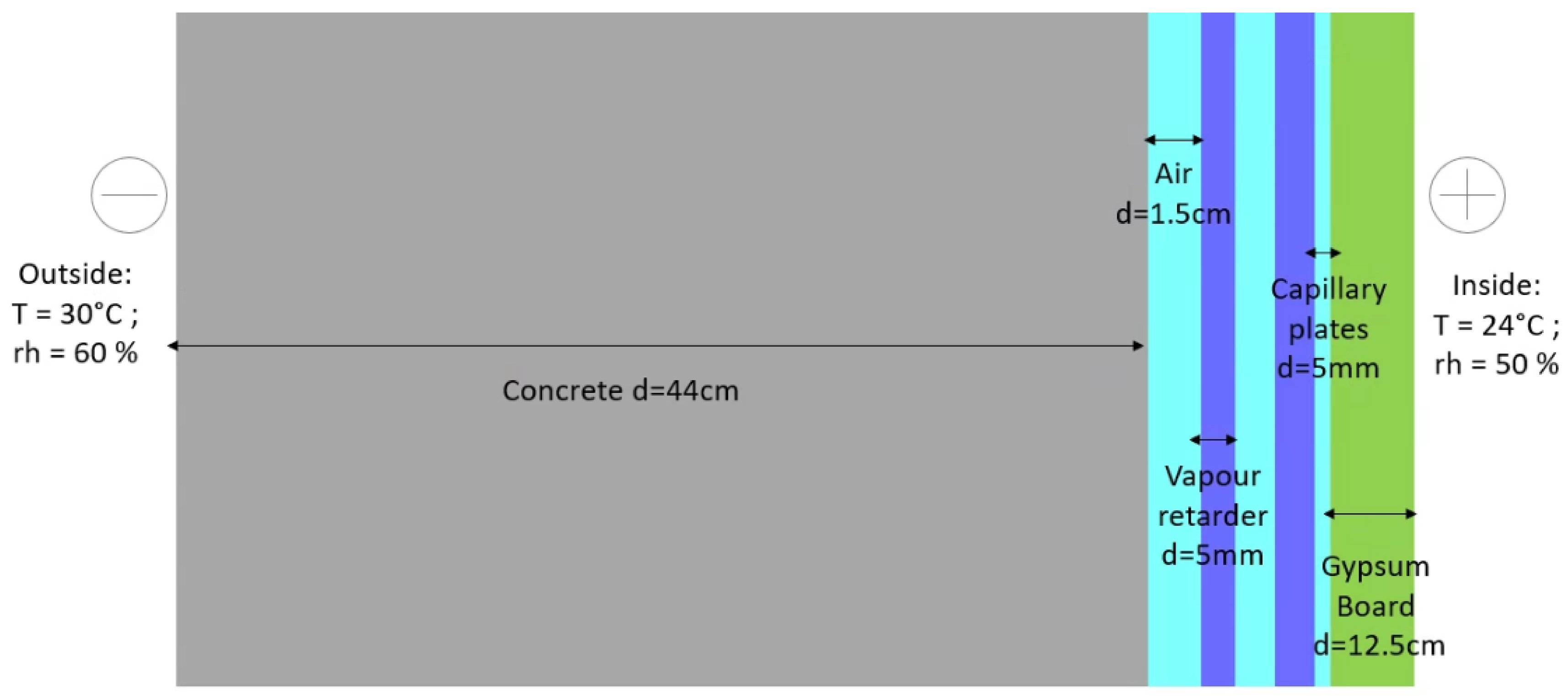

Fig. 1. *Wall construction S-3. Outer wall is slag concrete*

Results not considering moisture transfer

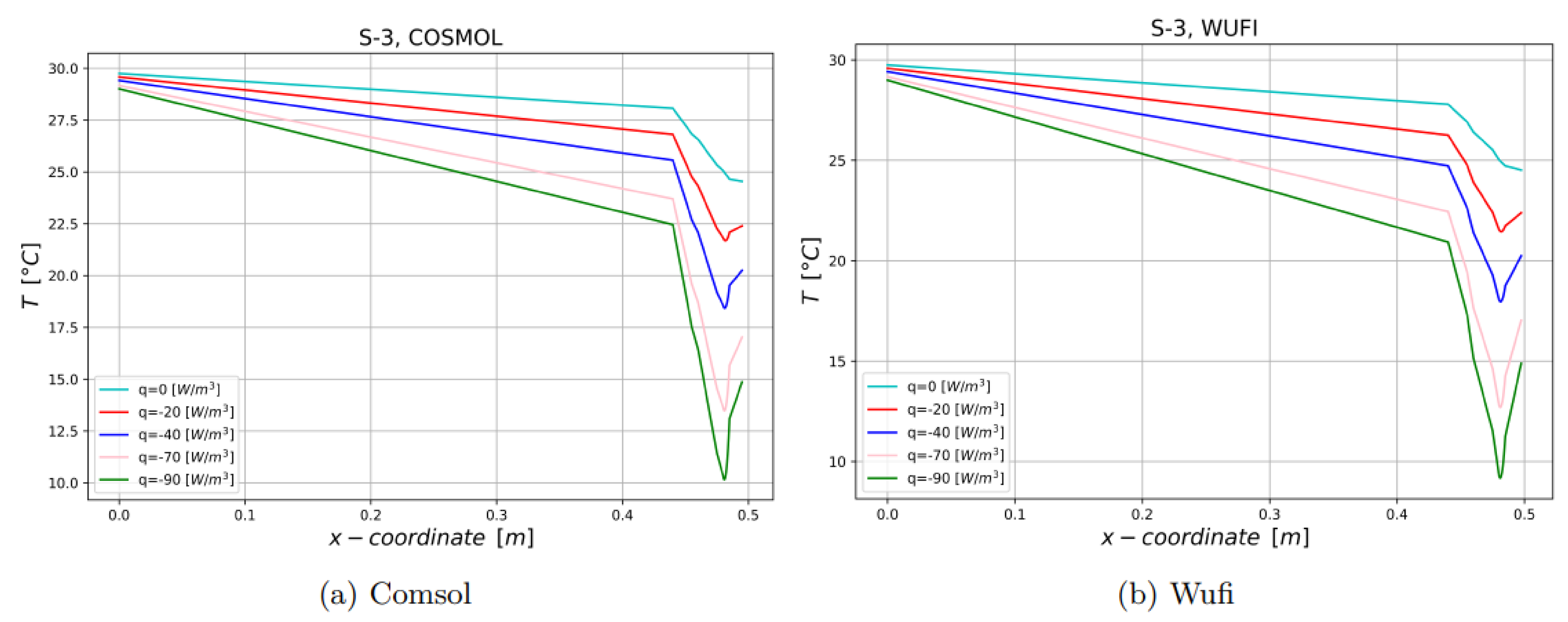

Fig. 2. *Temperature depending on the coordinate, changing the heat output of the capillary. Construction S-3*

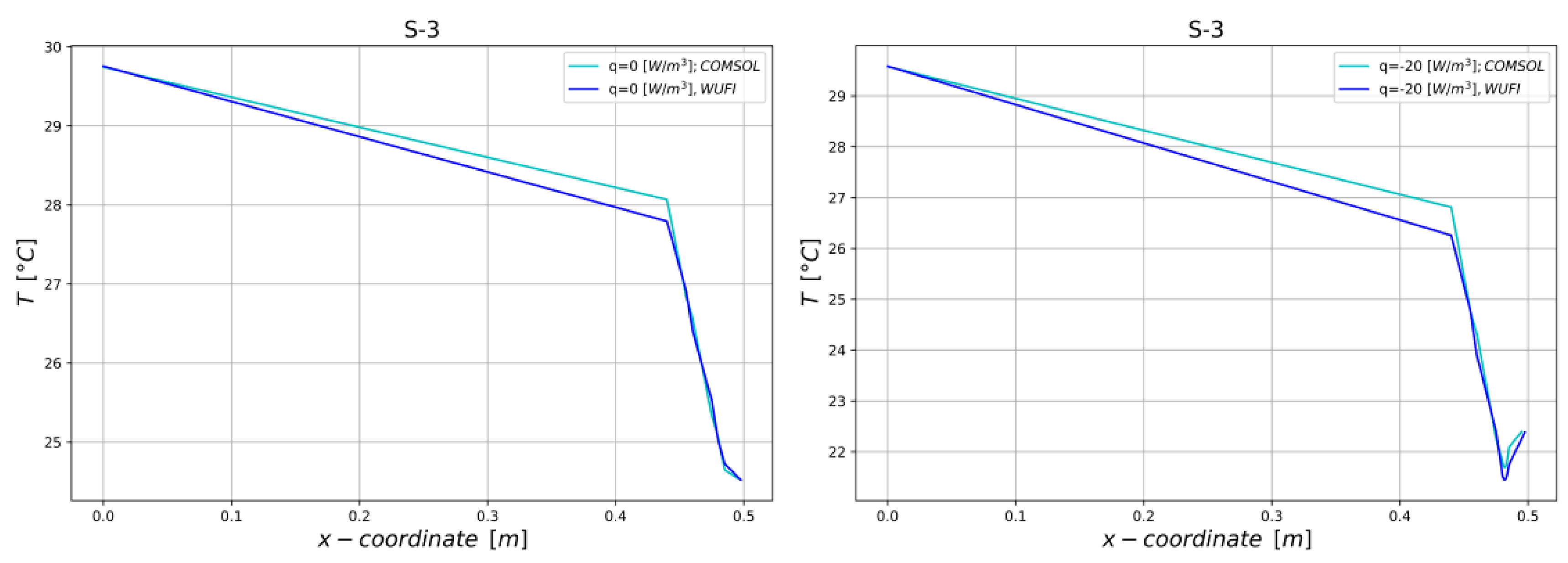

Fig. 3. *Temperature distribution in structure S-3 depending on the program used - Comsol (light blue), Wufi (dark blue)*

Results

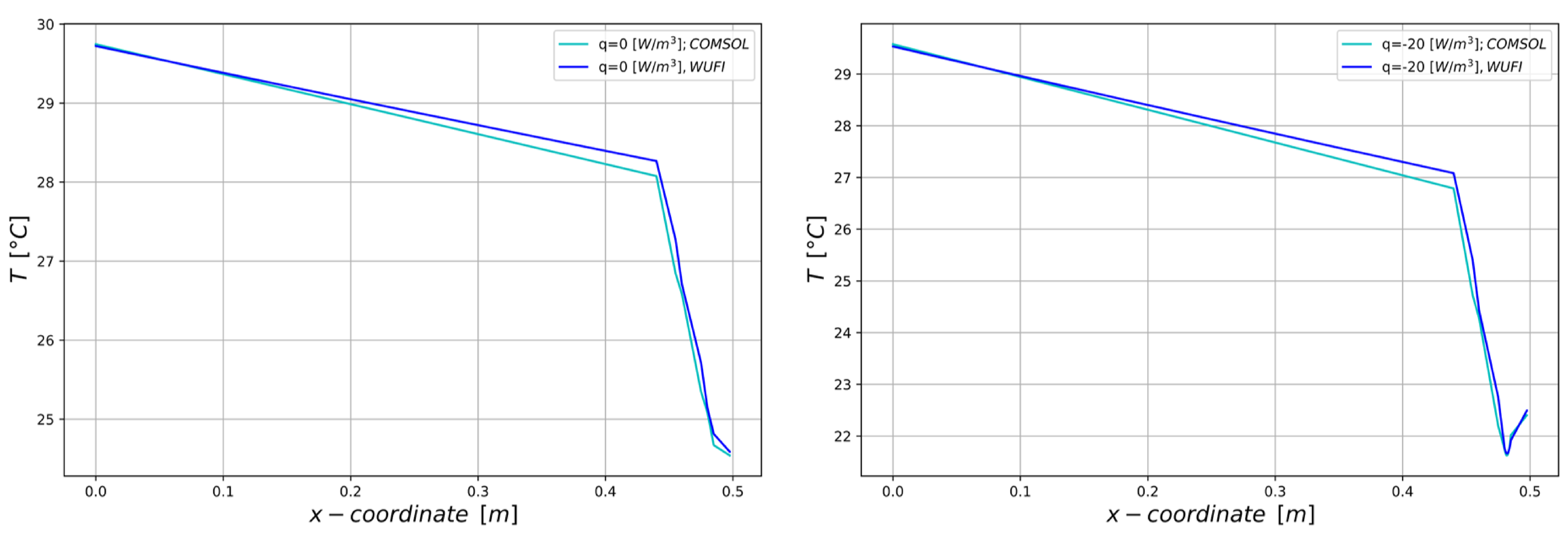

Fig. 4. *Temperature distribution in structure S-3 depending on the program used - Comsol (light blue), Wufi (dark blue), taking into account humidity*

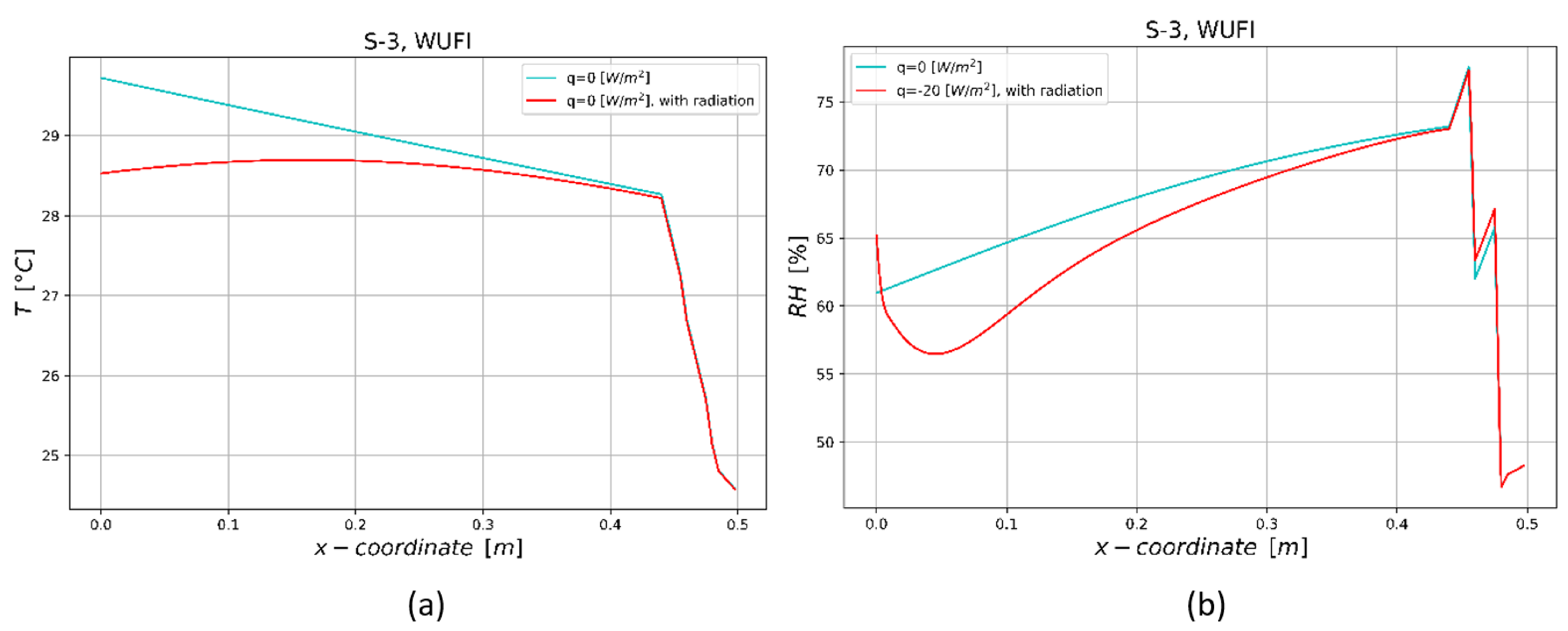

Fig. 5. *Temperature depending on the coordinate (a) and relative humidity distribution (b), taking into account sun radiation (red) and without (blue). Construction S-3*

Conclusions

Numerical modeling results show that there is no risk of mold when the capillary system is used as a cooling system in exactly these used structural models at certain capillary system capacities. More attention should be paid to the air layer, where the cooling capillary system and the largest temperature difference in the entire structure are located. As can be seen in Fig.2. , no more than -70\ W/m^2 heat flux should be ensured, otherwise there is a risk of mold in these wall structure. Experimental measurements will be used to validate and adjust both numerical models.

Acknowledgement

This work has been financially supported by the European Regional Development Fund project “Development and approbation of complex solutions for optimal inclusion of capillary heat exchangers in nearly zero energy building systems and reduction of primary energy consumption for heating and cooling” (1.1.1.1./19/A/102).

Modelling for Materials Processing
Rīga, September 2023

Optical imaging of MHD bubble flow in a Hele-Shaw liquid metal cell

Aleksandrs Jegorovs*, Mihails Birjukovs, Andris Jakovičs
University of Latvia, Jelgavas street 3, Riga LV-1004, Latvia *aleksandrs.jegorovs@lu.lv

Introduction

In some industrial metal processing methods, bubbles are injected into molten metal to enhance mixing, facilitate inclusion flotation [1], or to regulate flow. Understanding bubble flow and interactions in these magnetohydrodynamic (MHD) systems is vital for advancing metal processing. However, studying bubbly liquid metal flows, especially when numerous bubbles are present, is challenging for both numerical and experimental methods. Optical imaging approach [2] offers an affordable alternative to X-ray/neutron radiography [3]. This method is applicable when bubbles are confined within a vessel with a gap smaller than the bubble diameter (Fig. 1). This approach is cost-effective, easy to replicate, promotes more bubble interactions, simplifies data processing, provides excellent resolution, and is compatible with external magnetic field systems.

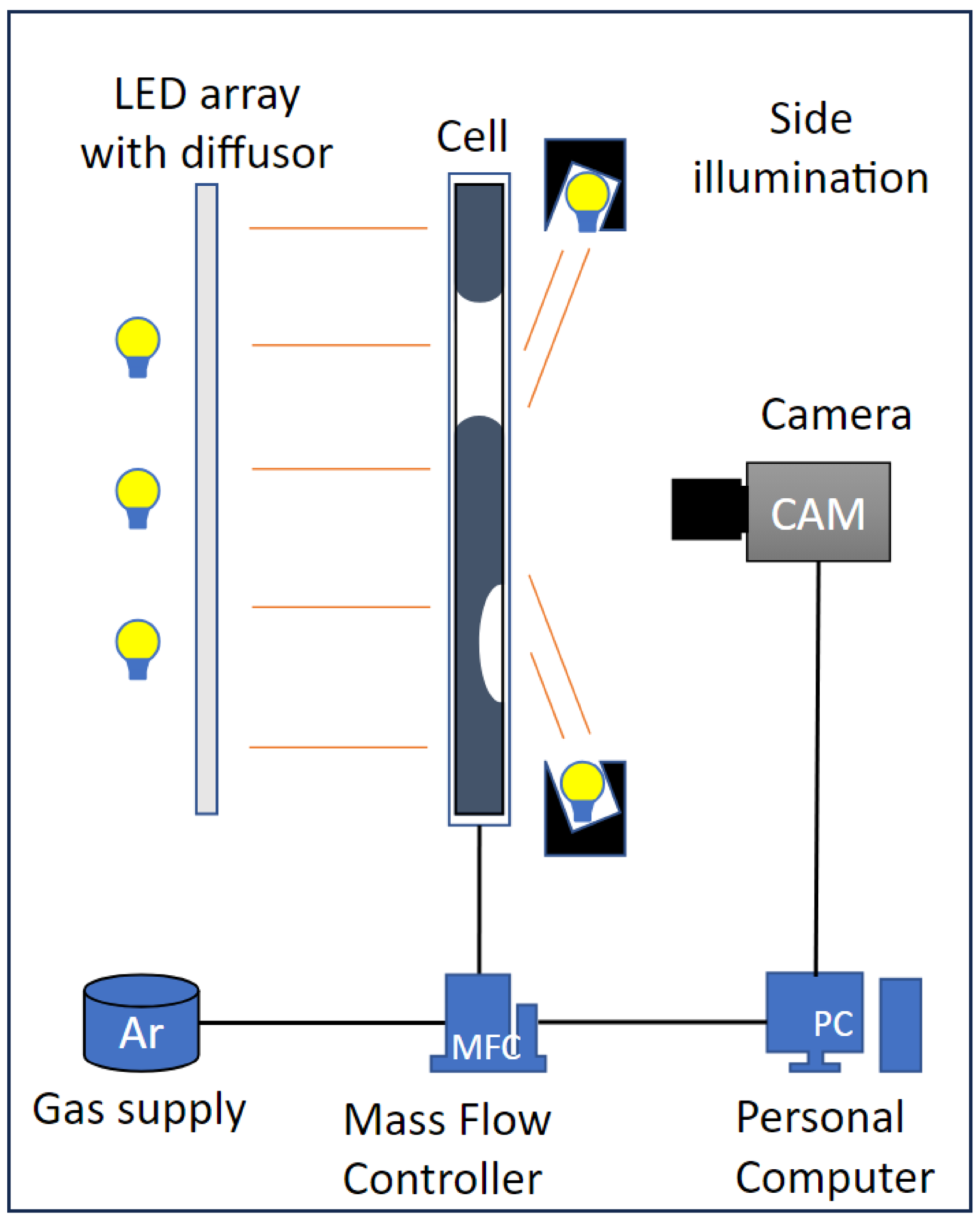

Fig. 1. *Optical experiment scheme.*

Experimental setup

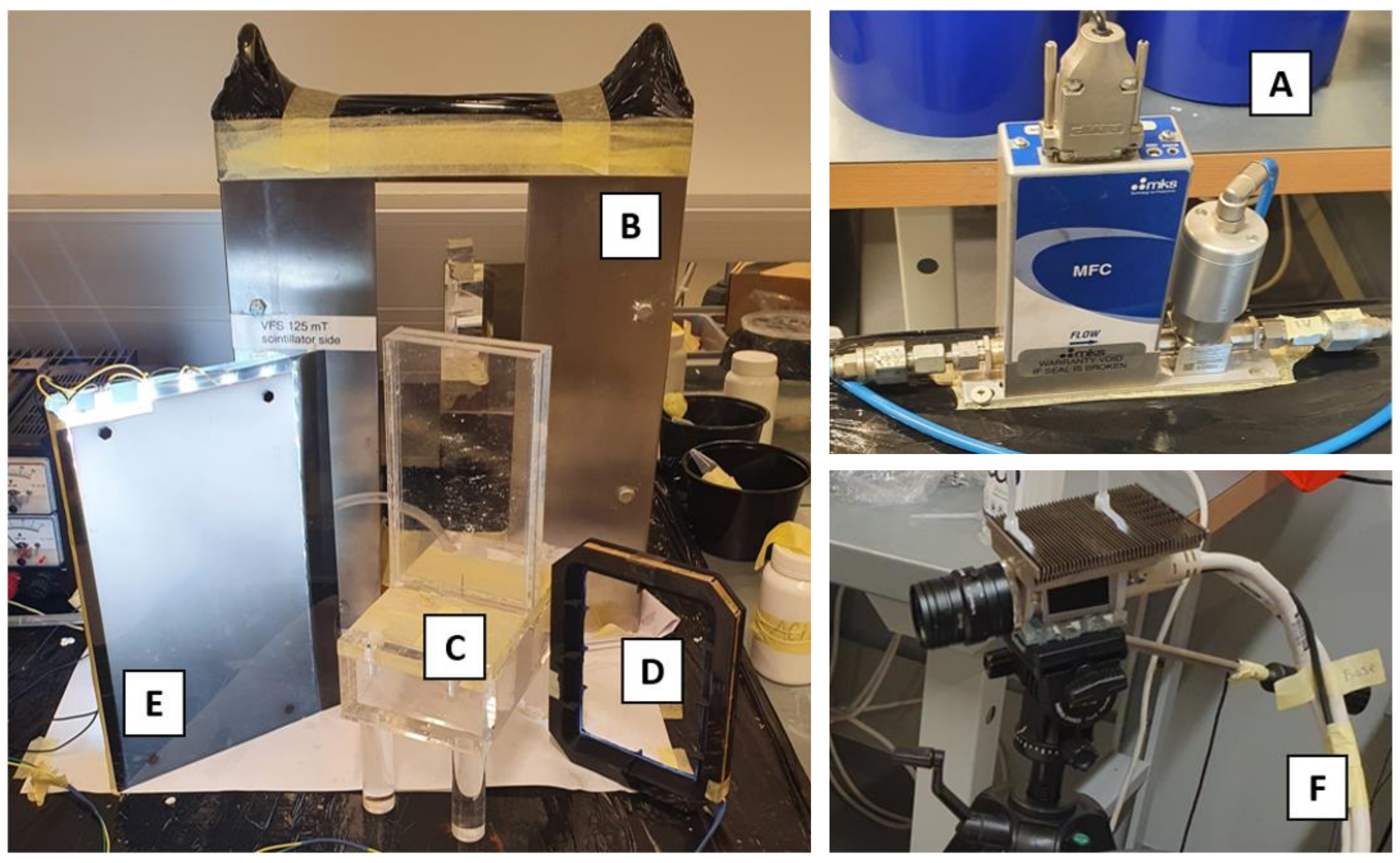

Fig. 2. *Optical experimental setup. A – Mass flow controller; B – One of external magnetic field systems; C – Hele-Shaw cell for liquid metal; D – Frontal/sideways illumination; E – Background illumination; F – High speed camera.*

Setup. Argon bubbles are injected into glass/acrylic Hele-Shaw cell (Fig. 2 C) filled with GaInSn alloy. Vessel's internal dimensions are 160×88×3 mm³ which ensures that most of bubbles are in contact with both vessel's walls and can be resolved using background illumination (Fig. 2 E). Fraction of bubbles are travelling next to single wall. Cases where bubbles travel next to front wall are resolved using sideways illumination (Fig. 2 D). Gas flow rate is controlled by MKS mass flow controller (Fig. 2 A). Setup can be studied under external magnetic field of longitudinal or transversal to bubble path direction and different strengths (example of a system at Fig. 2 B). Bubble trails are recorded using Basler acA2000-340km camera (greyscale, 2 MP, CMOS, 350 fps).

Data processing

Image processing. Images are cropped, binarized using static threshold value, small artifacts are removed using morphological opening and/or closing. Contours, which represent wh ole bubbles or bubble parts, are extracted from binarized image, filtered by size and position.

Contour data analysis. In ord er to restore trajectories, all neighboring (time-wise) frames pairs are analyzed for contour spatial proximity or overlap.

Connections between object on two subsequent frames, established during this process, are added as an 'edges' to a graph. Graph approach allows us to find an uninterrupted bubble trajectories and events of splits and merges via notion of node connectivity. Cases where connections are not uniquely resolved are subjected to tests for bubble's "pseudo momentum and mass conservation".

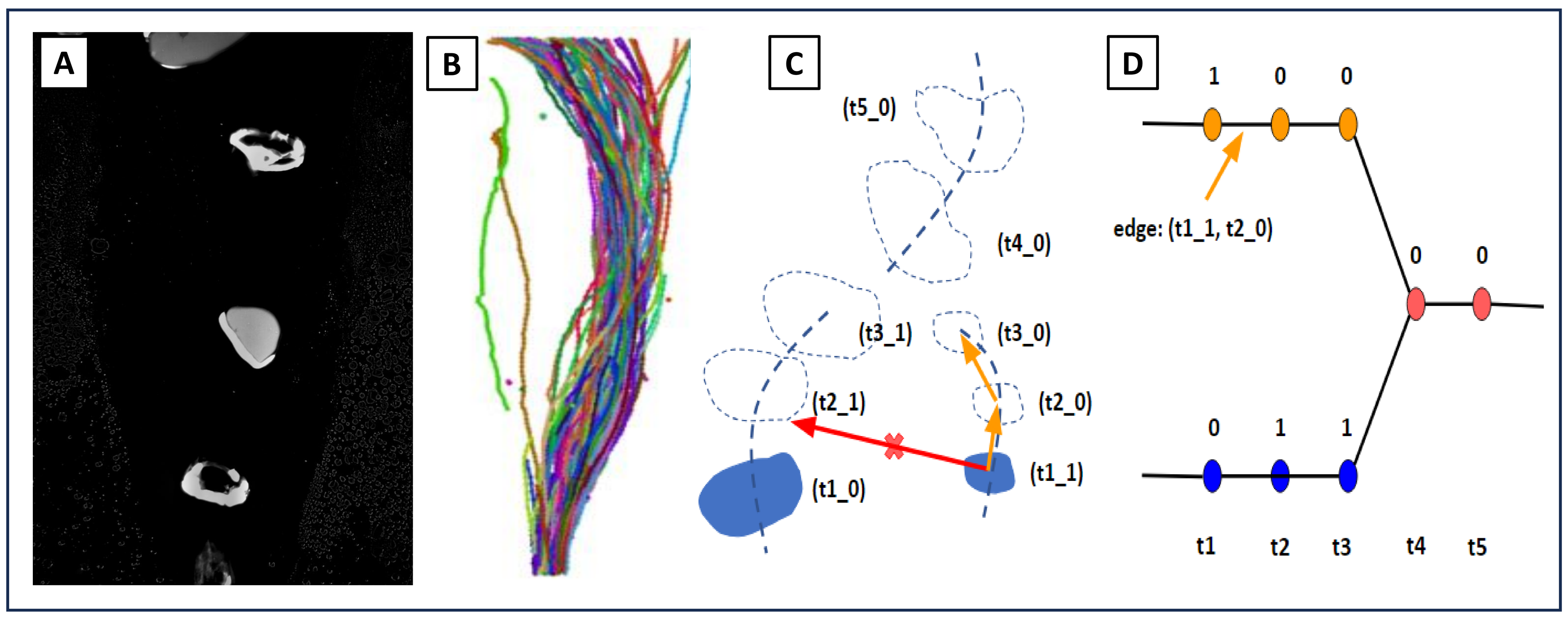

Fig. 3. *A – Example of an image of a bubble chain after minor pre-processing. B – Processed paths of many bubble centroids. C – Trajectory reconstruction methodology. Hypothetical merge event. Each pair of time steps is analyzed to establish bubble identity/connection. D – Graph representation of merge event.*

References

[1] Zhang, L., & Taniguchi, S. (2000). Fundamentals of inclusion removal from liquid steel by bubble flotation. In International Materials Reviews (Vol. 45, Issue 2, pp. 59–82). Informa UK Limited. https://doi.org/10.1179/095066000101528313

[2] Klaasen, B., Verhaeghe, F., Blanpain, B., & Fransaer, J. (2014). A study of gas bubbles in liquid mercury in a vertical Hele-Shaw cell. In Experiments in Fluids (Vol. 55, Issue 1). Springer Science and Business Media LLC. https://doi.org/10.1007/s00348-013-1652-x

[3] Keplinger, O., Shevchenko, N., & Eckert, S. (2017). Validation of X-ray radiography for characterization of gas bubbles in liquid metals. In IOP Conference Series: Materials Science and Engineering (Vol. 228, p. 012009). IOP Publishing. https://doi.org/10.1088/1757-899x/228/1/012009

Conclusions

The presented method enables the study of quasi-2D MHD flow under an applied external magnetic field. Experimental setup is cheap and simple. Image data processing uses only rudimentary methods. Graph based trajectory analysis approach is simple and intuitive. Current pipeline allows to analyze simple bubble trajectories and merge/split events. Further work is aimed at gathering more general statistics.

Modelling for Materials Processing
Rīga, September 2023
UNIVERSITY OF LATVIA
Leibniz Universität Hannover
Institute of Numerical Modelling

Numerical modelling of heating and melting of metal in industrial direct current electrical arc furnace

Sergejs Pavlovs[1*], Andris Jakovics[1], Alexander Chudnovsky[2]
[1]Institute of Numerical Modelling, University of Latvia, 3 Jelgavas Street, Riga, LV-1004, Latvia *Sergejs.Pavlovs@lu.lv
[2]JSC LATVO, 53 Ganibu Dambis, Riga, LV-1005, Latvia

Industrial direct current (DC) electric arc furnace (EAF)

capacity 3.6 tons of steel

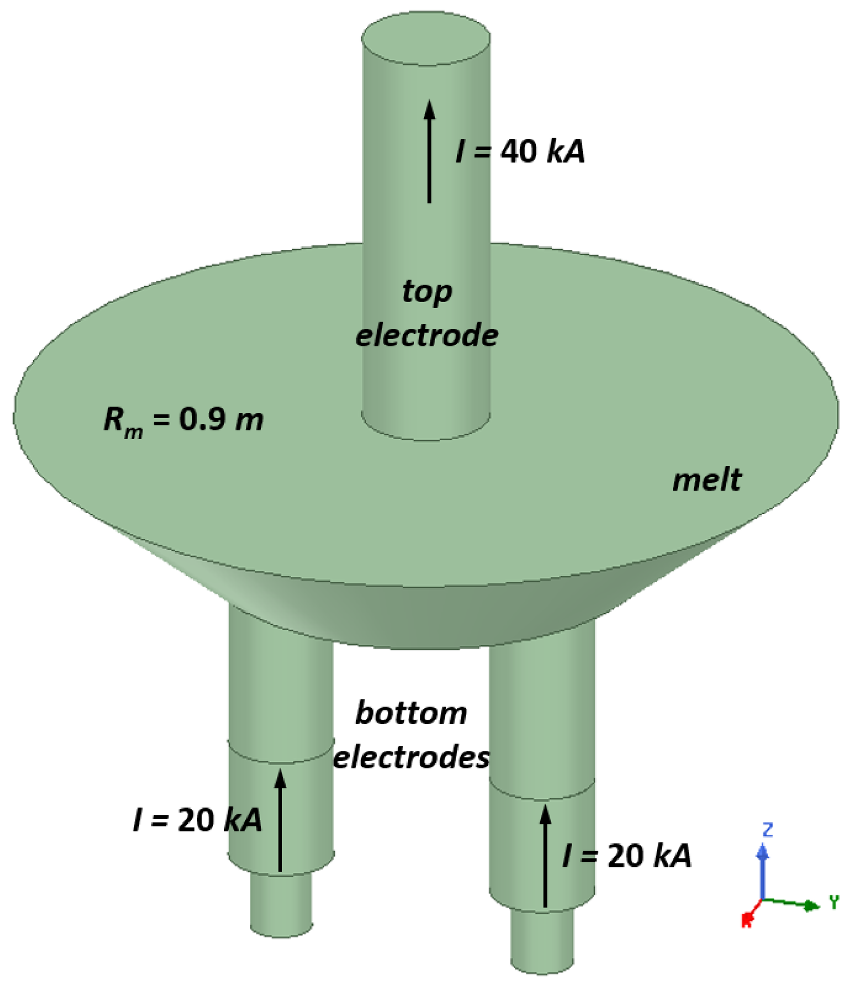

Linear distribution of liquid (ξ_l) and solid (ξ_s) fractions in mushy zone [2]

$$\xi_l = 1 - \xi_s \qquad \Pi = 1 - \xi_s = \xi_l$$

$$\xi_s(T) = \begin{cases} 0 & \text{for } T \geq T_{liquidus} \\ \dfrac{T_{liquidus} - T}{2T_{liquidus}} & \text{for } T_{liquidus} > T \geq T_{solidus} \\ 1 & \text{for } T < T_{solidus} \end{cases}$$

Governing equations

enthalpy (H) and porosity (Π) approach

$$\frac{\partial \rho}{\partial t} + \nabla(\rho \boldsymbol{V}) = 0$$

$$\frac{\partial(\rho \boldsymbol{V})}{\partial t} + \frac{\partial(\rho V_i V_j)}{\partial x_j} = -\nabla p + \eta \Delta \boldsymbol{V} + \rho \boldsymbol{g}(1 - \beta \Delta T) + \boldsymbol{J} \times \boldsymbol{B} + \boldsymbol{f}_{mush} - \frac{\partial\left(\rho \overline{V'_i V'_j}\right)}{\partial x_j}$$

Momentum sink $\boldsymbol{f}_{mush}$ in mushy zone due to reduced porosity derived using Kozeny-Carman equation [1]

$$\boldsymbol{f}_{mush} = -\frac{(1-\xi_l)^2}{\xi_l^3 + \epsilon} \cdot \boldsymbol{V} \cdot A_{mush}$$

$$\boldsymbol{V} = \begin{cases} \boldsymbol{V_l} & \text{for liquid phase} \\ (1-\xi_s)\boldsymbol{V}_l = \xi_l \boldsymbol{V}_l & \text{for the mushy region} \\ \boldsymbol{V}_s = 0 & \text{for solid phase} \end{cases}$$

$$\frac{\partial(\rho H)}{\partial t} + \nabla(\rho H \boldsymbol{V}) = \nabla(\lambda \nabla T) + \frac{|\boldsymbol{J}|^2}{\sigma} - \frac{\partial\left(\rho \overline{V'_i h'}\right)}{\partial x_i}$$

$$H = h + \Delta H \qquad h = h_{ref} + \int_{T_{ref}}^{T} c_p dT$$

$$\Delta H(T) = \begin{cases} \Delta H = h_{melting} & \text{for } T \geq T_{liquidus} \\ [1 - \xi_s(T)]h_{melting} = \xi_l(T) h_{melting} & \text{for } T_{liquidus} > T \geq T_{solidus} \\ 0 & \text{for } T < T_{solidus} \end{cases}$$

Heat balance equation: estimation of heat flux supplied through spot of arc [3]

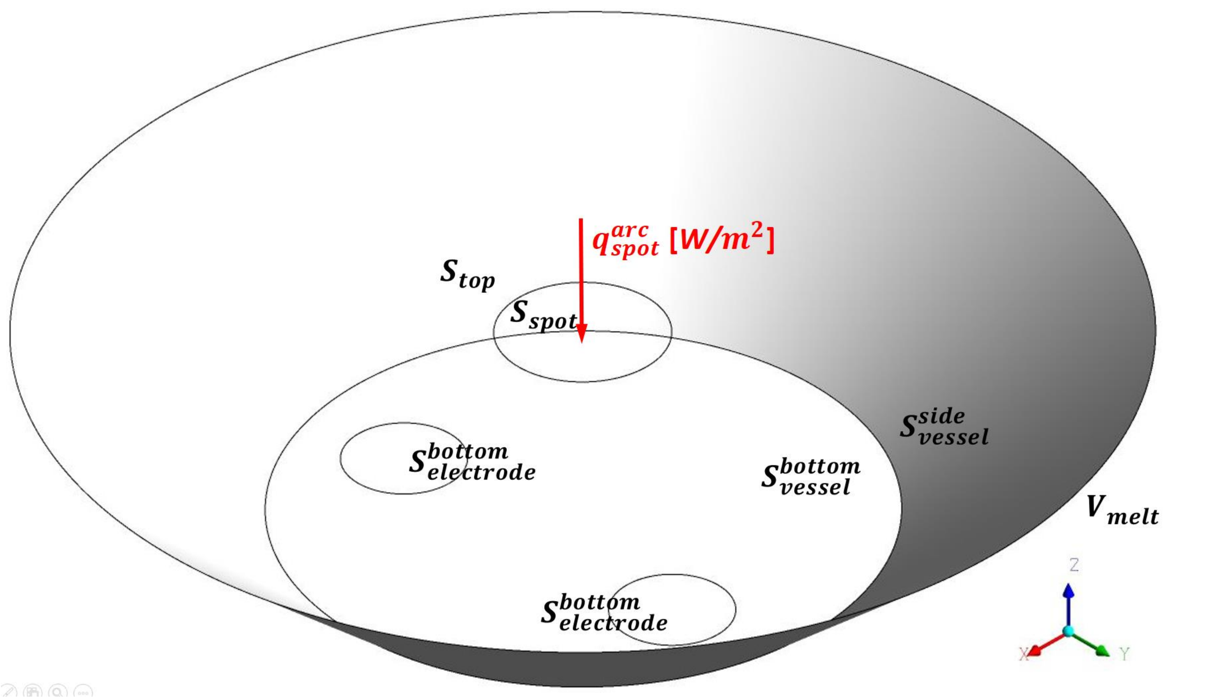

$$q_{spot}^{arc} S_{spot} = \frac{\sigma_{SB}\left(T_{melting}^4 - T_{cover}^4\right) S_{top}}{1/\varepsilon_m + 1/\varepsilon_{cover} - 1} + \frac{\alpha_{conv}\lambda_f}{\lambda_f + \alpha_{conv} d_f}\left(T_{melting} - T_a\right) S_{vessel} +$$

$$+ \frac{2\lambda_e}{d_f}\left(T_{melting} - T_{cooling}\right) S_{electrode}^{bottom} + \frac{c_m \rho_m V_{melt}\left(T_{melting} - T_{initial}\right)}{\Delta t} +$$

$$+ \frac{h_{melting} V_{melt}}{\Delta t} - \int_{V_{melt}} \frac{|\boldsymbol{J}|^2}{\sigma} dV$$

$$q_{spot}^{arc} \sim 5.1 \cdot 10^7 \ W/m^2$$

Melting acceleration due to intensification of electrovortex flow

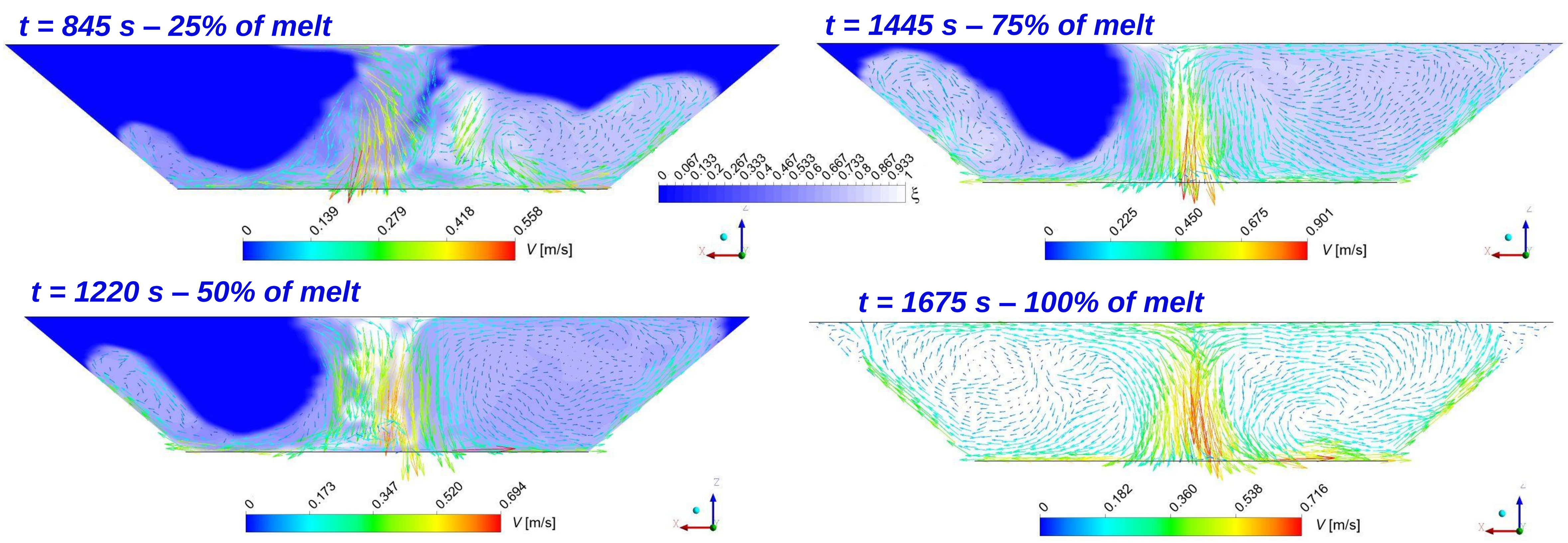

$$T_{solidus} = T_{liquidus} \qquad A_{mush} \sim 10^3 \ kg/(m^3 \cdot s)$$

Estimation of melting integral time

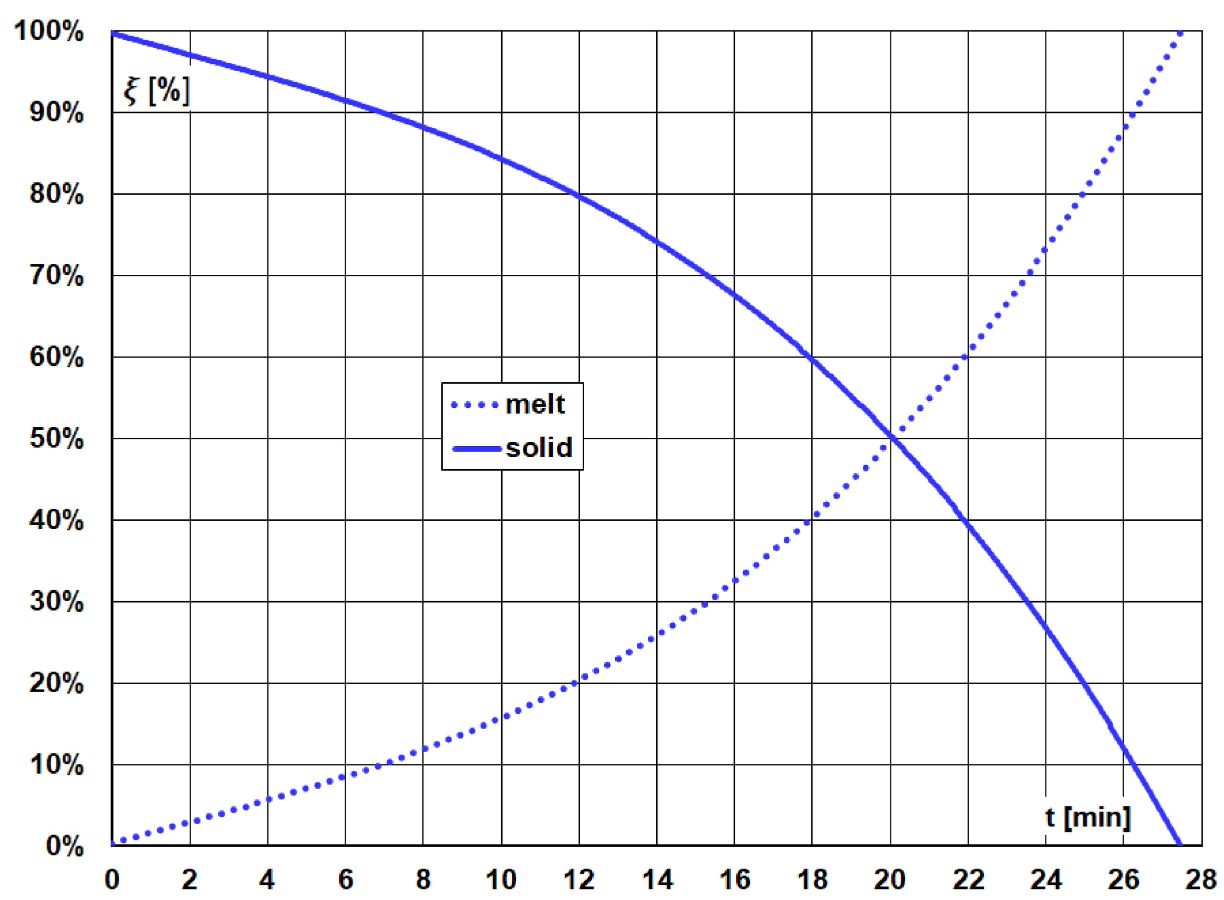

References

[1] Carman, P.C. (1937) Fluid flow through granular beds. Transaction of Institute of Chemical Engineers, 15, 150–156.
[2] Voller, V.R., Prakash, C. (1987) A fixed grid numerical modelling methodology for convection-diffusion mushy region phase-change problems. International Journal of Heat and Mass Transfer, 30 (8), 1709–1719.
[3] Pavlovs, S., Jakovics, A., Chudnovsky, A. (2023) Numerical modelling of heating and melting of metal in mini industrial direct current electrical arc furnace. Proceedings of International Symposium on Heating by Electromagnetic Sources (HES-23), Padua, Italy, ID31:1–8.

Acknowledgements

EUROPEAN UNION
European Regional Development Fund

This work was funded under contract No. 1.1.1.1/18/A/108

"Development of numerical modelling approaches to study complex multiphysical interactions in electromagnetic liquid metal technologies"

Numerical Modelling of Feed Rod Melting Dynamics During Floating Zone Silicon Crystal Growth

Modelling for Materials Processing
Rīga, September 2023

Maksims Surovovs[1*], Jānis Virbulis[1]
1. Institute of Numerical Modelling, University of Latvia, Jelgavas street 3, Riga LV-1004, Latvia
*maksims.surovovs@lu.lv

Introduction

During floating zone (FZ) process, polycrystalline feed rod is heated by a high-frequency induction coil. The molten silicon forms a thin layer on the open melting front and travels down to the melt.

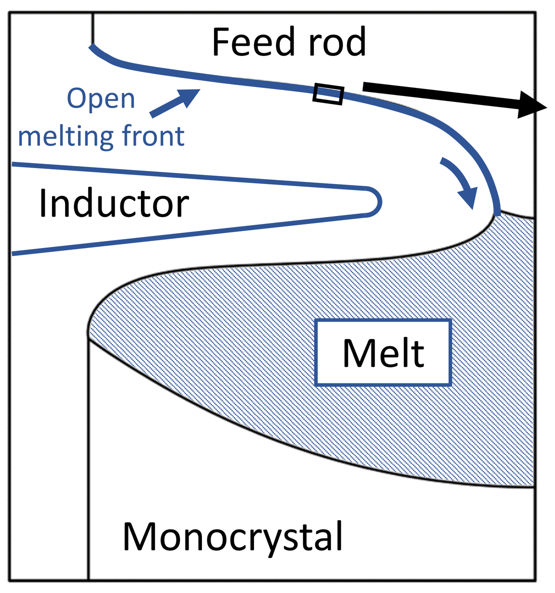

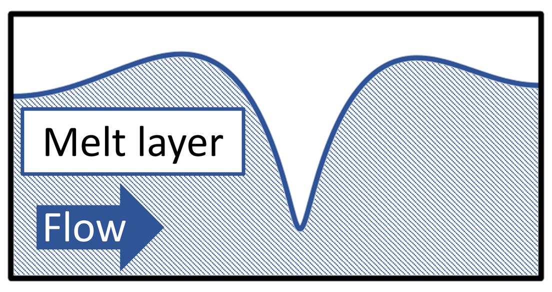

Fig. 1. Cross-section of the FZ process (left) and a close-up of the region with a single melting front structure

Motivation:
- Non-uniform melting of the feed rod during FZ process leads to inhomogeneous melting structures
- Local melting front structures are generally neglected in numerical simulations
- Results from quasi-stationary simulations [1] can improve the precision of the global model

Aim:
- Implementation of volume of fluid method to obtain transient shapes of phase boundaries based on quasi-stationary model results
- Investigation of time-dependent flow in the thin melt layer in regions with melting front structures, especially during the breaking of the fluid film

Reference case

The previously developed quasi-stationary model [1] was used to simulate a reference case, which can be used as initial geometry for the transient simulations.

interface slope angle	θ	5°
EM coil frequency	f	3.0 MHz
melt flow rate	Q	1.86 mm²/s
crystal growth rate	V_C	2.0 mm/min

Tab. 1. Parameters used in quasi-stationary simulations of the reference case.

- Melting front structures are not created in regions with a completely flat interface. An initial perturbation on the feed rod surface is required
- Initially defined perturbation is amplified
- Perturbation center is shifted slightly due to non-stationary effects

Fig. 4. The initial shape and the converged quasi-stationary solution for the fluid film thickness h

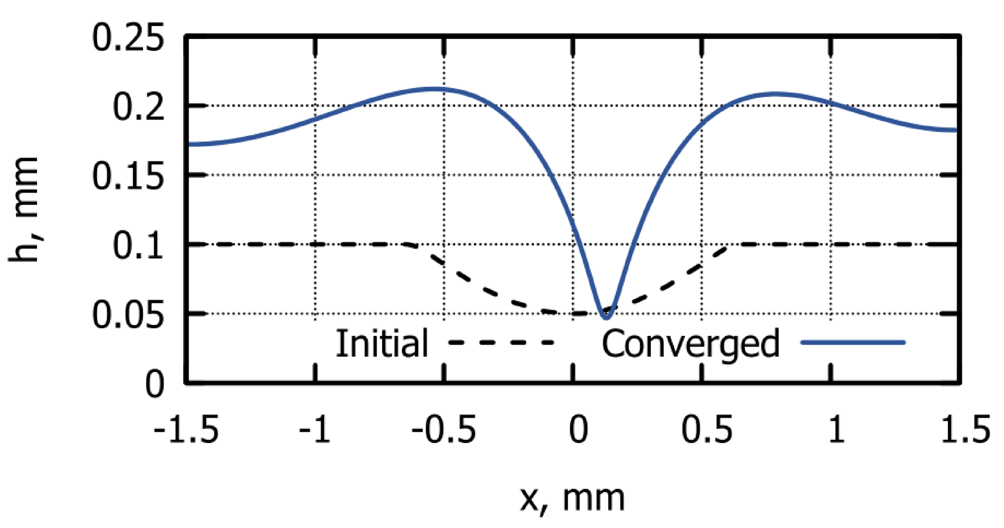

References

1. M. Surovovs, M. Sjomkane, J. Virbulis & G. Ratnieks. *Abstracts of Seventh European Conference on Crystal Growth*, Paris, France, 196 (2022).
2. H. G. Weller, G. Tabor, H. Jasak & C. Fureby. *Computers in physics* 12, 620–631 (1998).
3. G. Ratnieks. *Modelling of the Floating Zone Growth of Silicon Single Crystals with Diameter up to 8 Inch*, PhD thesis (University of Latvia, 2007).

Quasi-stationary simulations

- Local 2D model with one perturbation is considered
- Physical fields are coupled and solved in `OpenFOAM` [2] using the appropriate solvers
- The process is repeated iteratively until convergence of the open melting front shape is obtained
- Shape of phase boundaries is calculated separately; geometry is updated between the iterations

Fig. 2. The overall scheme of the quasi-stationary model

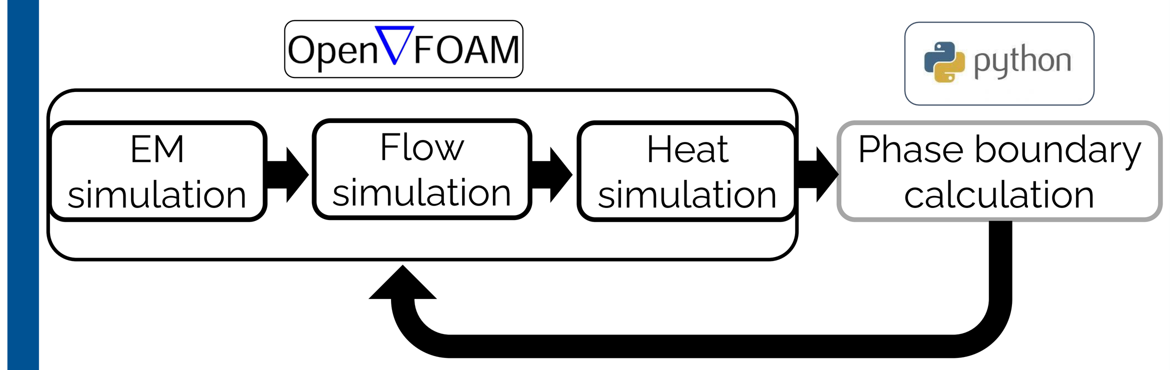

Phase boundary calculation

Calculated separately for each point after the physical field simulations. Interfaces are shifted based on the resulting heat fluxes and the balance of the surface tension and the resulting pressure from the hydrodynamic simulations. Curvature of the free surface is obtained using the parametrization of the point coordinates.

$$c\Delta y = q_L - q_{cr} - q_S, \qquad \Delta y = c'(p_L + \gamma k),$$
$$\Delta y = c'\left(\lambda_L \nabla T_L - \rho L v_f - \lambda_S \nabla T_S\right),$$

Δy – resulting shift (< 1μm)
c, c' – shift scale factor
L – specific latent heat
v_f – feed rod pushing rate
γ – surface tension
k – free surface curvature
q_L – heat flux from the melt
q_S – heat flux from the polycrystal
q_{cr} – heat of crystallization
$\lambda_{L,S}$ – heat conductivity
p_L – pressure inside the melt
$\nabla T_{L,S}$ – gradient at the interface

Reference case: main results

- Strong Lorentz force near the free surface; force vectors are slanted near the curved regions of the melting interface
- Very small temperature increase over the melting point with minimal values near the perturbation
- Highest flow velocity (≈ 6 cm/s) near the peak; two low-velocity vortexes can be seen

Fig. 5. From top to bottom: Lorentz force, temperature increase over the melting point, flow velocity

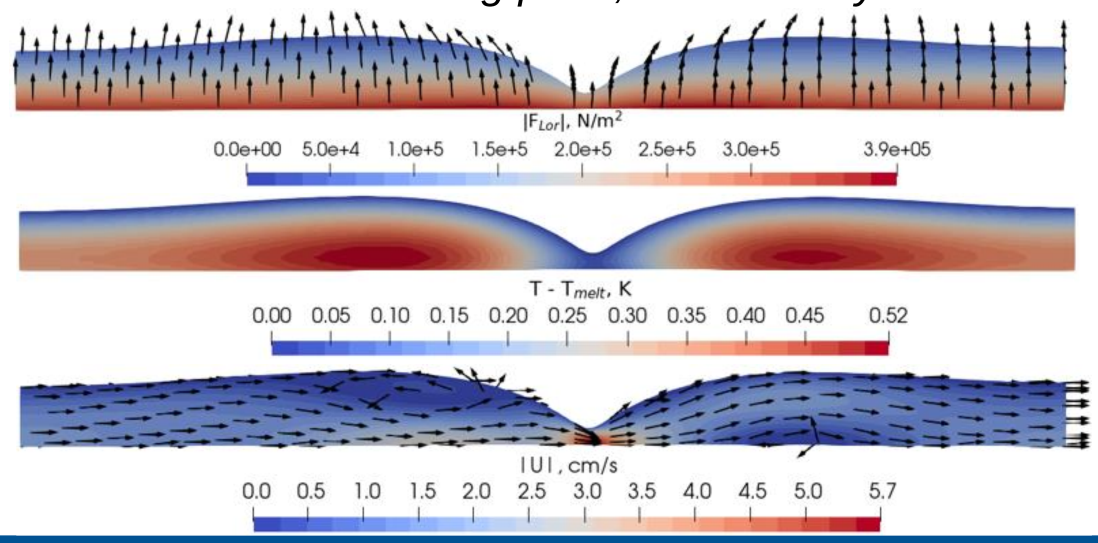

Summary and conclusions

- Quasi-stationary case with selected process parameters was simulated to obtain realistic perturbation shape for use in volume of fluid simulations
- Transient simulations show that the melt flow is re-established after the breaking of the thin film for the considered process parameters
- Transient simulations result in an unstable solution; quasi-stationary state is not obtained
- Increase of melt viscosity results in increased layer thickness, but the presence of the interface perturbation results in discrepancy with analytical values

Transient model

- `OpenFOAM` [2] implementation of volume of fluid method `interFoam` is used
- Only hydrodynamic simulations are performed, heat transfer and EM field not considered
- Constant melting interface shape is defined according to quasi-stationary results of the reference case
- Simulations are started after the film breaking; melt is present only on one side of the perturbation
- The flow is re-established after breaking
- Solution is unstable and displays large velocity values; quasi-stationary state is not reached

Fig. 3. Melt velocity distribution at different time steps

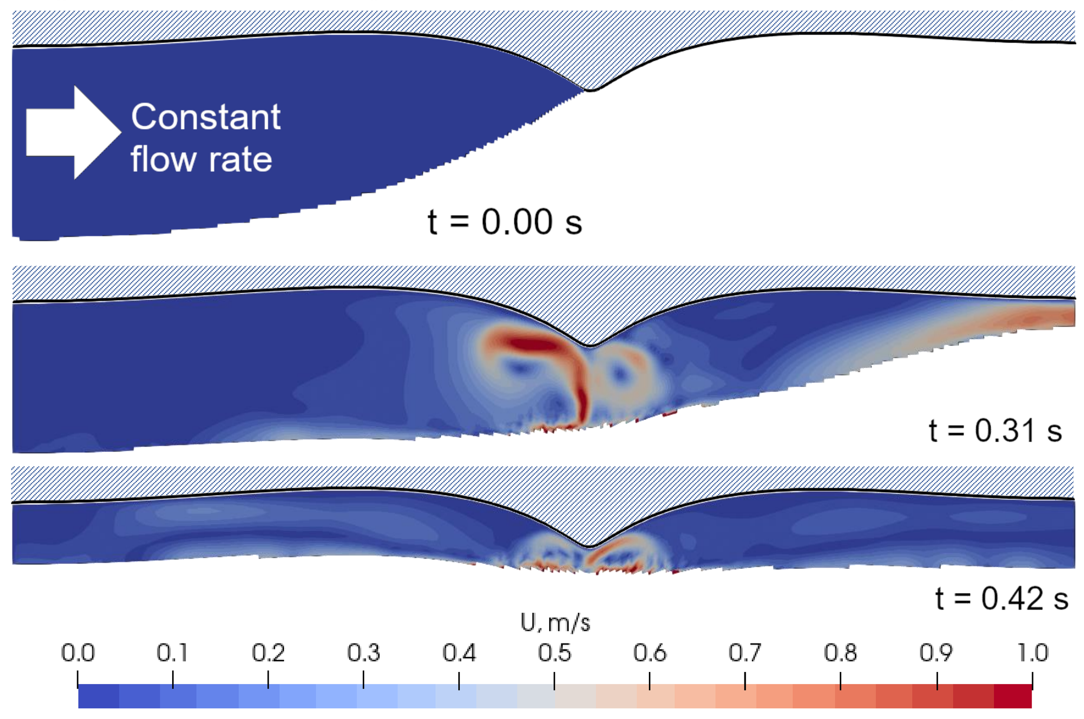

Comparison between models

- Significantly higher maximum velocity near the peak in case of transient simulations
- Quasi-stationary simulations result in effectively flat free surface, which is not the case with transient model due to element size
- Transient model results in an unstable solution with significant differences between time steps

Fig. 6. Flow velocity distribution inside the melt layer for quasi-stationary (top) and transient (bottom) model

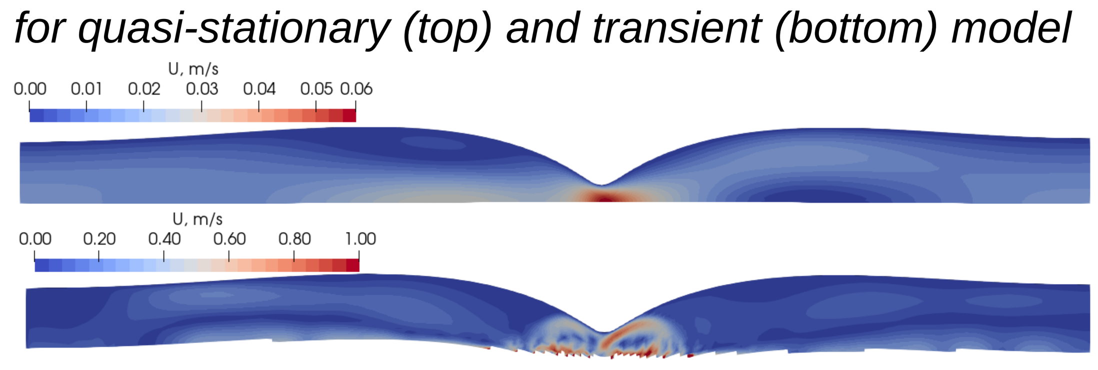

Model verification

Different viscosity values were tested and compared to analytical melt thickness h [3] for model verification:

$$h = \left[\frac{3\eta\rho_S V_F (R_F^2 - r^2)}{2\rho_L^2 g \sin\theta(r) \cdot r}\right]^{1/3}$$

η – dynamic viscosity
V_F – feed rod move rate
R_F – feed rod radius
ρ – density
$\vec{g}$ – free fall acceleration
θ – interface slope angle

- Increase of melt viscosity results in an increase of average melt layer thickness, but there is a slight discrepancy with theoretical values due to the presence of the interface perturbation

Fig. 7. Comparison of average melt layer thickness as a function of viscosity with the analytical expression

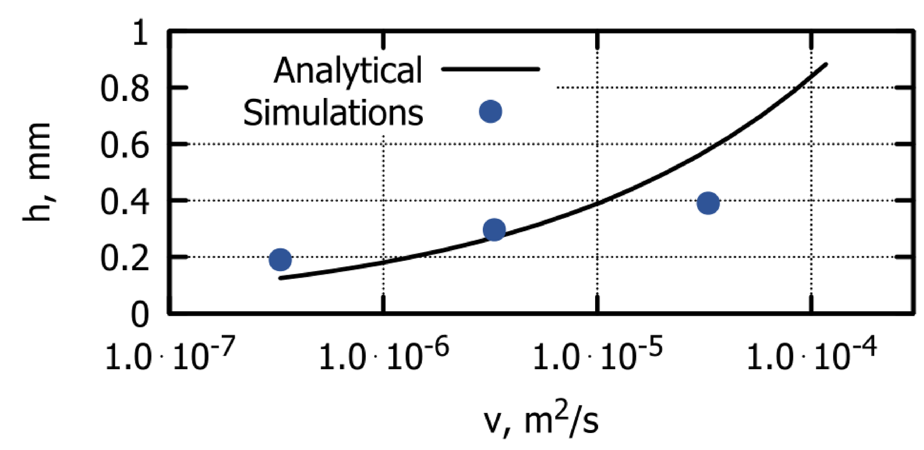

Modelling for Materials Processing
Rīga, September 2023

UNIVERSITY OF LATVIA | Leibniz Universität Hannover | Institute of Numerical Modelling

Effect of dopant boundary conditions on crystal resistivity during floating zone growth of silicon crystals

Staņislavs Luka Stroževs*, Kirils Surovovs, Jānis Virbulis

University of Latvia, Jelgavas Street 3, Riga LV-1004, Latvia *stanislavs_luka.strozevs@lu.lv

Introduction

The floating zone (FZ) method is a crucible-free crystal growth method, which is used to grow high-purity silicon crystals. In this method, the feed rod is melted by high-frequency inductor, the molten silicon flows downwards and forms a molten zone, which then crystallizes into a single crystal. The method is realized in a chamber filled with argon under pressure of at least 1.5 bar [1]. To get a desired value of electrical resistivity in the grown crystal, dopants (typically phosphorus P in the form of phosphine PH_3) are added to gas through a tube (see Fig. 1, left).

There are multiple approaches to model dopant transport in the melt. For example, on the free surface (FS) different boundary conditions have been used for dopant concentration (C): uniform $C = 1$ arb. u. [2] or non-uniform $\frac{\partial C}{\partial n}$ that corresponds to the doping gas inlet tube position [3]. These conditions ensure that dopants get into the melt through the free surface. In reality, however, they can also evaporate [4], especially for low argon pressures [5, 6]. The aim of the work is **to test the effect of wide range of the possible C boundary conditions on the crystal resistivity profiles**.

Another system parameter, that is not precisely known, is the Marangoni coefficient (M) – surface tension derivative with respect to temperature – which depends on atmosphere composition, e.g., oxygen content.

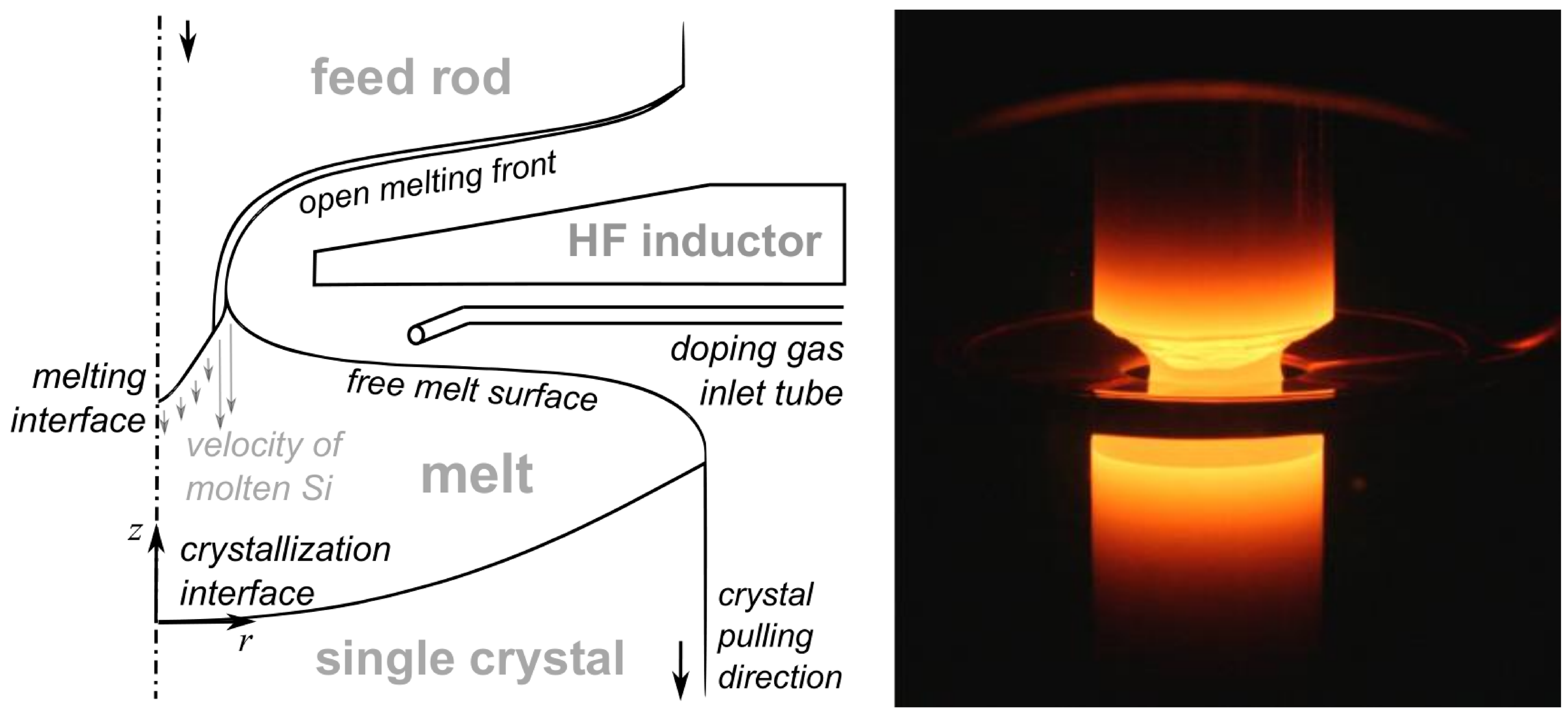

Fig. 1. An axially symmetrical sketch of the FZ method (left) and a photograph of an experiment (right) by Wünscher et al. [7].

Mathematical model

The melt flow and dopant transport in melt is simulated with the *OpenFOAM* hydrodynamic solver [2]. It assumes fixed phase boundaries and uses the Navier–Stokes equation (transient, incompressible, laminar) for melt velocity, including Marangoni, electromagnetic and buoyancy forces. C transport is modelled by solving the convection-diffusion equation

$$\frac{\partial C}{\partial t} + (\mathbf{v} \cdot \nabla)C = D_C \Delta C$$

with the boundary conditions mentioned in Tab. 1. On the crystallization interface, segregation boundary condition [2] is used in all cases.

Approach	melting front, inner part	melting front, outer part	free surface
A: non-uniform non-negative C flux on the FS	$C = 0$	C from gas	Non-negative C flux from gas
B: uniform negative C flux on the FS	$C = 0$	C from gas	$\frac{\partial C}{\partial n} = g_{FS} < 0$
C: uniform fixed C on the FS	$C = 0$	$0 \leq C = C_{MI} < 1$	$C = 1$ arb. u.

***Tab. 1.** The tested approaches (sets of boundary conditions for C).*

Results: C evolution in time

Due to the time-dependent nature of the process, it was important to ensure that the average value of C is converged: C oscillates around a steady value as in Fig. 2, right.

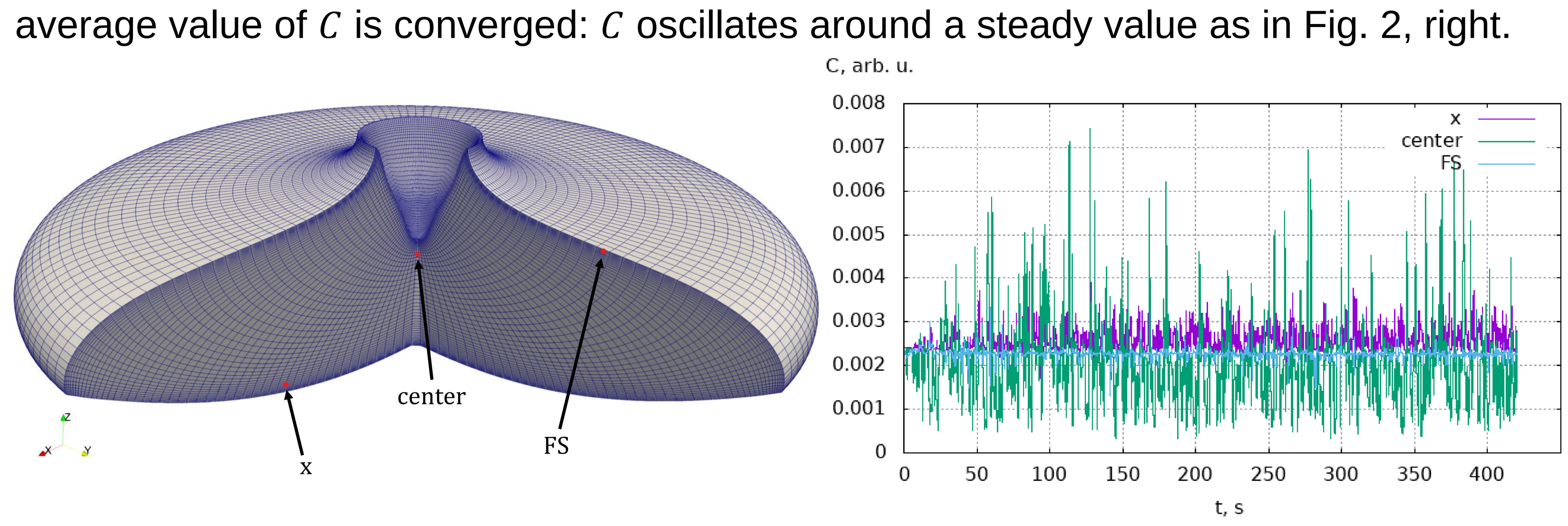

Fig. 2. A sketch of probe points (left) and dopant concentration evolution in time at these points during the simulation of the case with $g_{FS} = -1$ arb. u. (right).

Results: different boundary conditions for C

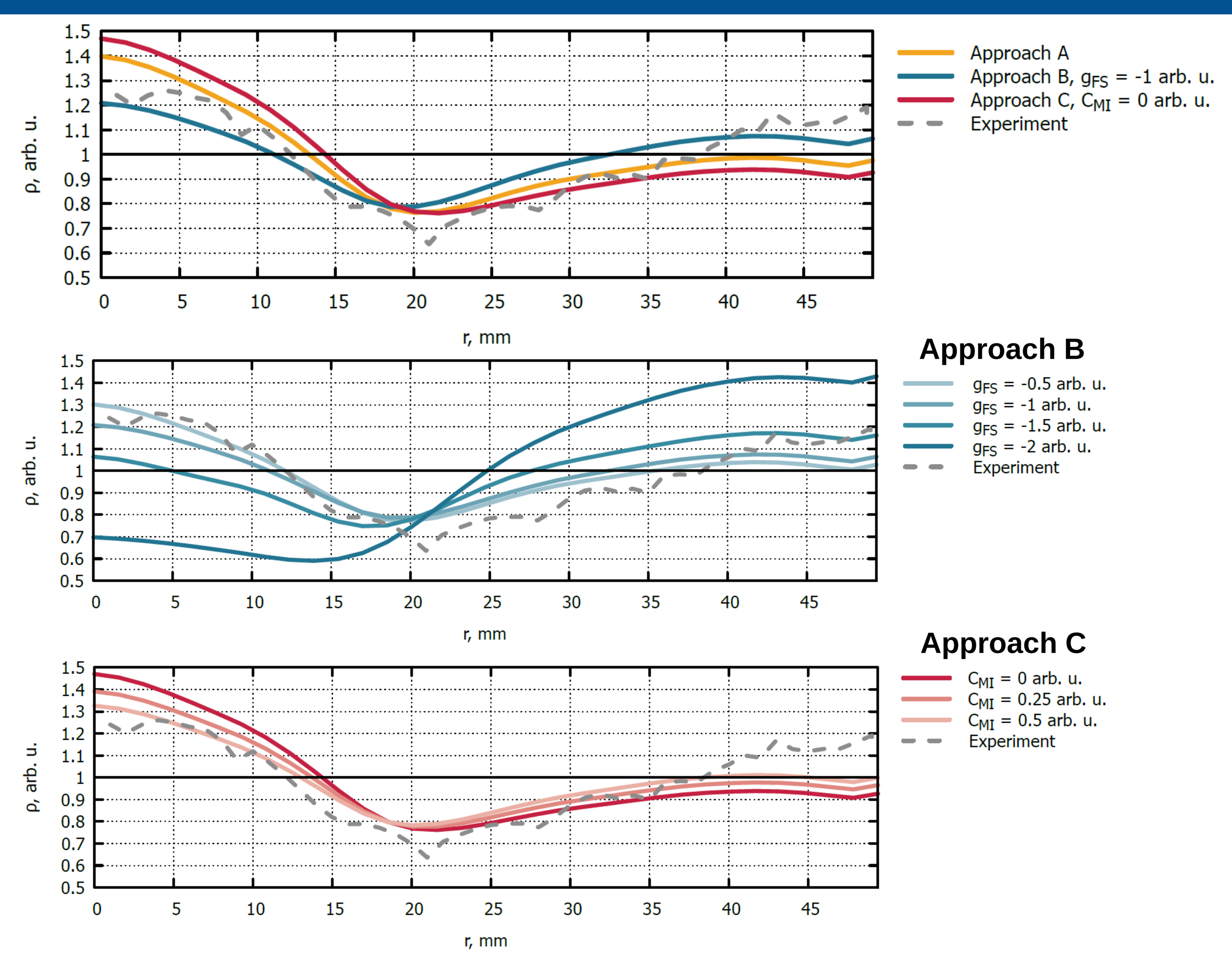

Resistivity ($1/C$) normalized profiles corresponding to different approaches (top), different g_{FS} values (middle) and different C_{MI} values (bottom). Experiment data is taken from [8].

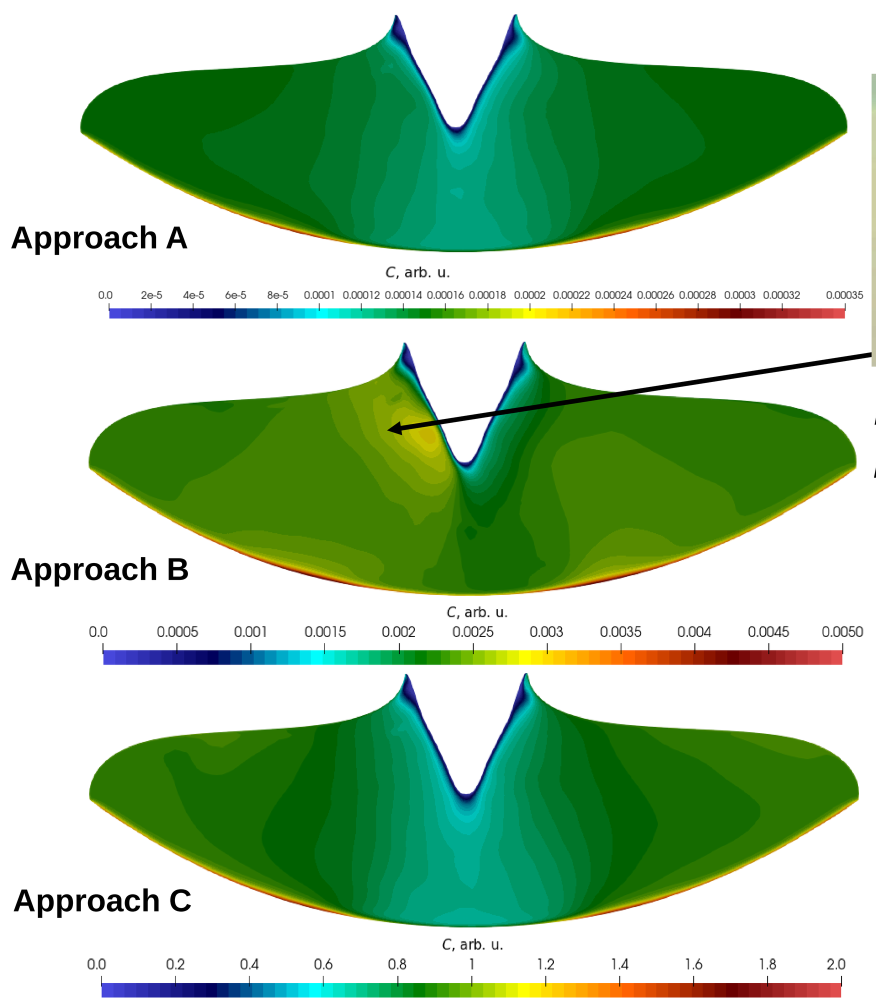

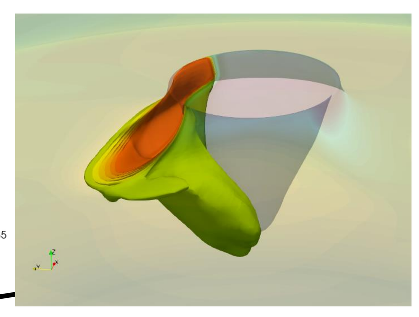

Local maximum of C near the melting front.

Time-averaged dopant concentration: Approach A (top), Approach B with $g_{FS} = -1$ arb. u. (middle), Approach C with $C_{MI} = 0$ (bottom).

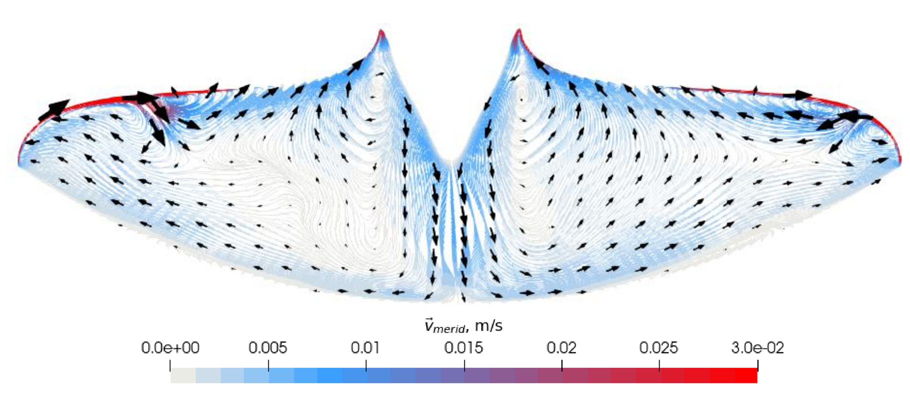

Time-averaged velocity field.

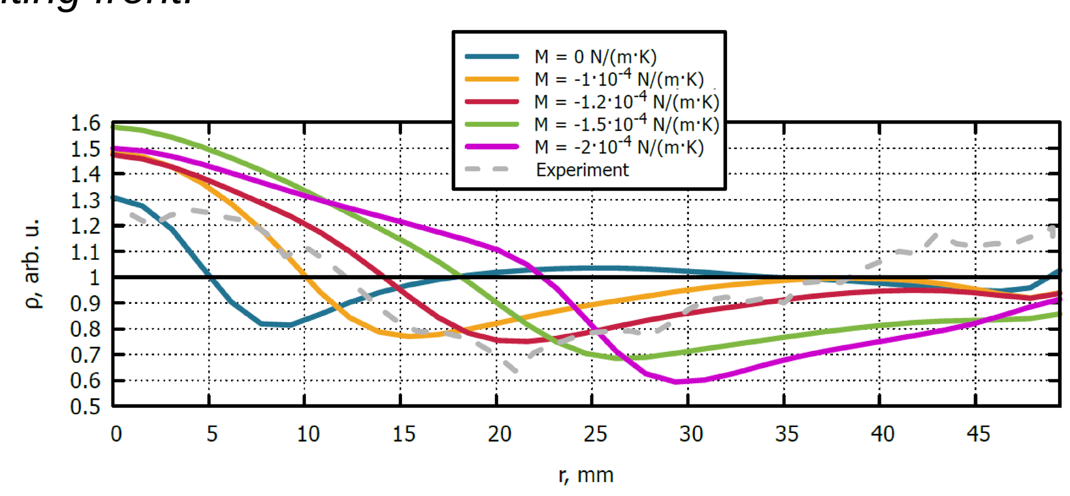

Resistivity normalized profiles corresponding to the Approach A with different values of the Marangoni coefficient M. Based on these results, $M = -1.2 \cdot 10^{-4}$ N/(m·K) was used in simulations with other approaches.

References

[1] Zobel et al., Modelling for Materials Processing, 2017
[2] Lācis et al., Magnetohydrodynamics, Vol 46, 2020
[3] Sabanskis et al., Journal of Crystal Growth, Vol 457, 2011
[4] Li et al., IEEE Journal of Photovoltaics, Vol 8, 2018
[5] Zheng et al., Metallurgical and Materials Transactions A, Vol 42, 2011
[6] Zheng et al., Transactions of Nonferrous Metals Society of China, Vol 21, 2011
[7] Wünscher et al., Modelling for Electromagnetic Processing, 2008
[8] Rost et al., Journal of Crystal Growth, Vol 360, 2012

Conclusions

- The three considered approaches produce very similar C distributions in the melt, even though dopant flux on the FS is non-negative in Approaches A and C.
- In accordance with the previous studies, $M = -1.2 \cdot 10^{-4}$ N/(m·K) ensures a position of crystal resistivity minimum that corresponds to the experiment.
- With higher absolute values of g_{FS}, C at the outer part of the melt decreases, thus resistivity increases at the rim and decreases in the center.
- Higher values of C_{MI} produce a lower value of resistivity it the center.

Modelling for Materials Processing
Rīga, September 2023

UNIVERSITY OF LATVIA

Leibniz Universität Hannover

Influence of surface waves on liquid-to-gas mass transfer in molten silicon

G. Zageris*, V. Geza, S. Pavlovs
Institute of Numerical Modeling, University of Latvia, Jelgavas street 3, Riga LV-1004, Latvia *girts.zageris@lu.lv

Introduction

- For solar power purposes, solar grade silicon is required, but its production is costly.
- Silicon must be purified to attain solar grade purity. For boron, it is known that the rate of its removal depends on the surface and volume of the melt:

$$\ln\left(\frac{C_{\mathrm{B},0}}{C_{\mathrm{B},t}}\right) = k_{\mathrm{B}}\frac{St}{V}$$

- In this study, **a numerical model supports the idea that surface waves on the melt surface increase the rate of impurity removal**.

Numerical model

- Model is of an **axisymmetric cyllindrical tank**, gas blows over silicon melt (modeled **only as a boundary**). Fluid flow + mass transfer is modeled. Mass transfer obeys the following transport law:

$$\frac{\partial C}{\partial t} + \boldsymbol{u}\cdot\nabla C = D\nabla^2 C$$

- Boundary E (Fig. 1) can be deformed as a harmonic wave. Mass transfer of boron is modeled through it with Fickian diffusion. Concentration in the melt is assumed constant at all times.
- Parameter studies on surface wave amplitude, frequency and wavelength are performed, the outflow of boron with the bulk gas is determined and compared between cases.
- To verify the model, the special case of a stationary surface is compared with experimental data from literature in [1, 2]. Coefficient $k_{\mathrm{B}} = 1.9$ μm/s is attained, which agrees with the typical range.

Results

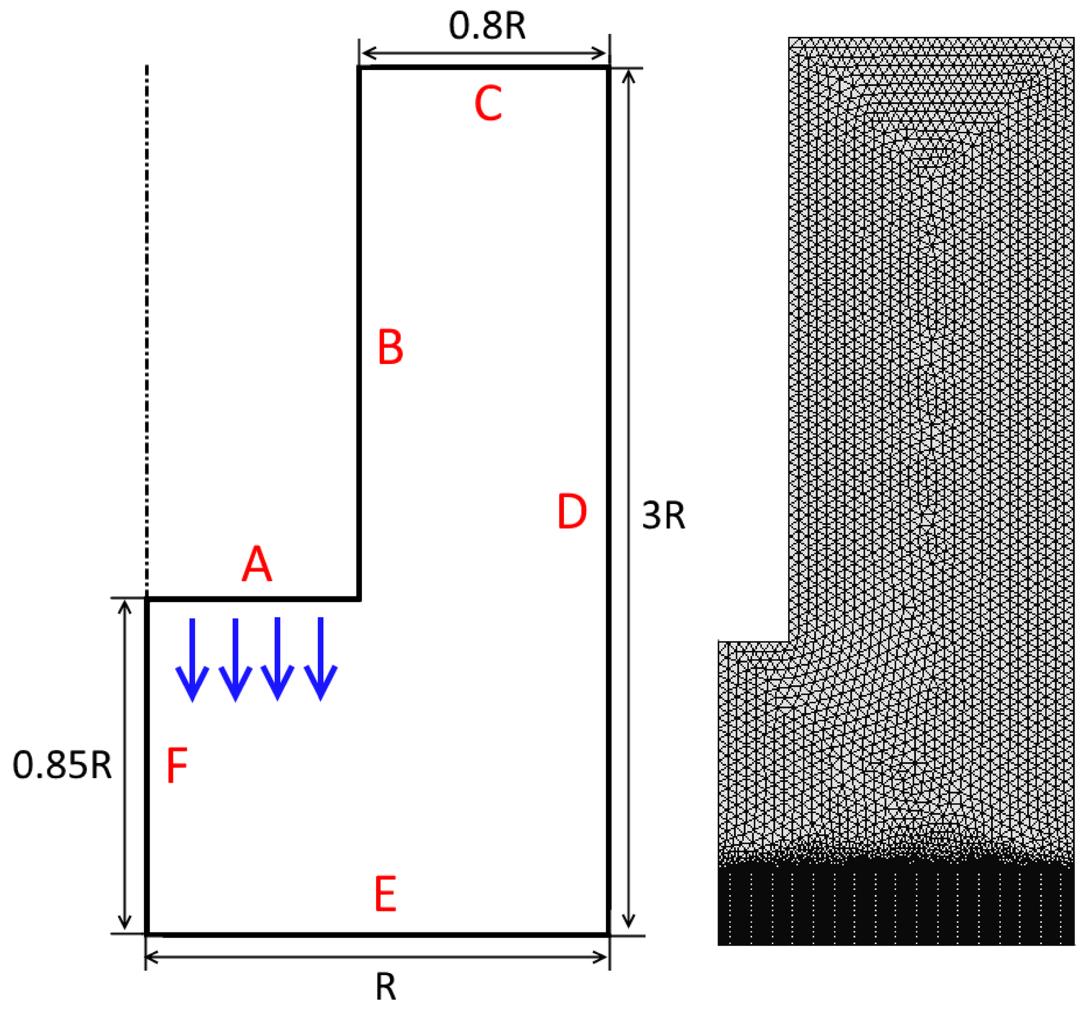

***Fig. 1.** Sketch of geometry and numerical mesh*

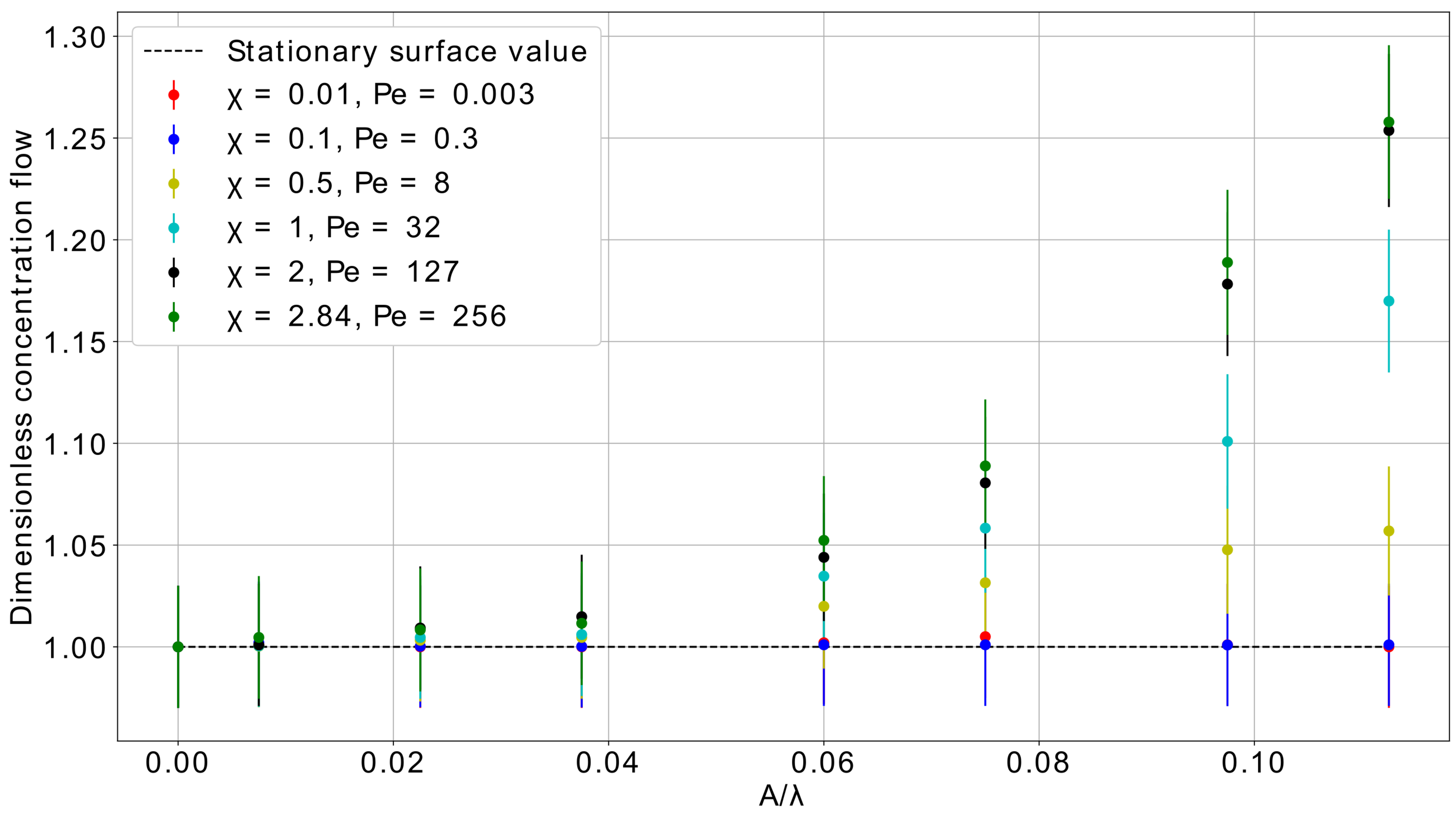

***Fig. 2.** Impurity outflow vs. wave amplitude for various χ values*

$$\chi = \frac{A}{2\sqrt{D_0 T}}$$

References

1. Sortland, Ø. and Tangstad, M. (2014) Boron removal from silicon melts by H2O/H2 gas blowing: mass transfer in gas and melt., *Metallurgical and Materials Transactions E*, vol. 1, no. 3, p. 211–225, 2014.
2. Sortland, Ø.S. (2015) Boron removal from silicon by steam and hydrogen, PhD thesis, Trondheim: Norwegian University of Science and Technology, October 2015

Conclusions

1. **A wavy surface does improve impurity removal rate.**
2. The effect is due to increased surface area, altered flow patterns near the melt surface and a change in the attack angle of the flow on the surface.
3. This effect is only present when the ratio of wave amplitude and characteristic diffusion length for impurities is above unity.

Modelling for Materials Processing
Rīga, September 2023

UNIVERSITY OF LATVIA

Leibniz Universität Hannover

Finite element method calculations coupled with circuit simulator

V. Geza[1], K. Bolotin[1*]
University of Latvia, Jelgavas street 3, Riga LV-1004, Latvia
*kirill.bolotin@lu.lv

Introduction

Modeling of electromagnetic systems using the finite element method (FEM) usually involves a number of simplifications, such as changes in geometry, the absence of some elements and boundary conditions. Usually fixed current or fixed voltage is used as source condition in numerical simulations. However, real conditions may be more complex and have a significant impact on the result.

However, real conditions are more complicated, as those can involve power conditioners, impedance matching and other electronic components. Also, power source can be power controlled (output is fixed power instead of fixed voltage/current). Furthermore, AC power source output frequency can depend on load impedance.

SPICE (Simulation Program with Integrated Circuit Emphasis) is an open source general purpose electronic circuit powerful simulator that allows to design and analyze various circuits, but it also has limitations, for example, modeling of magnetic circuits that describe the magnetic circuits of both electronic components and in electrical installations [1].

SPICE has three approaches to this problem: linear and non-linear inductance modeling, and magnetic coupling modeling. In the first and second cases, we are talking about the analysis of electronic components, for which many different parameters of resistance, capacitance and inductance are considered. The third case considers an ideal transformer consisting of several linear inductors [2].

Other possibility to tackle this problem is, again, coupling with FEM models where precise magnetization curve is taken into account.

Section 1

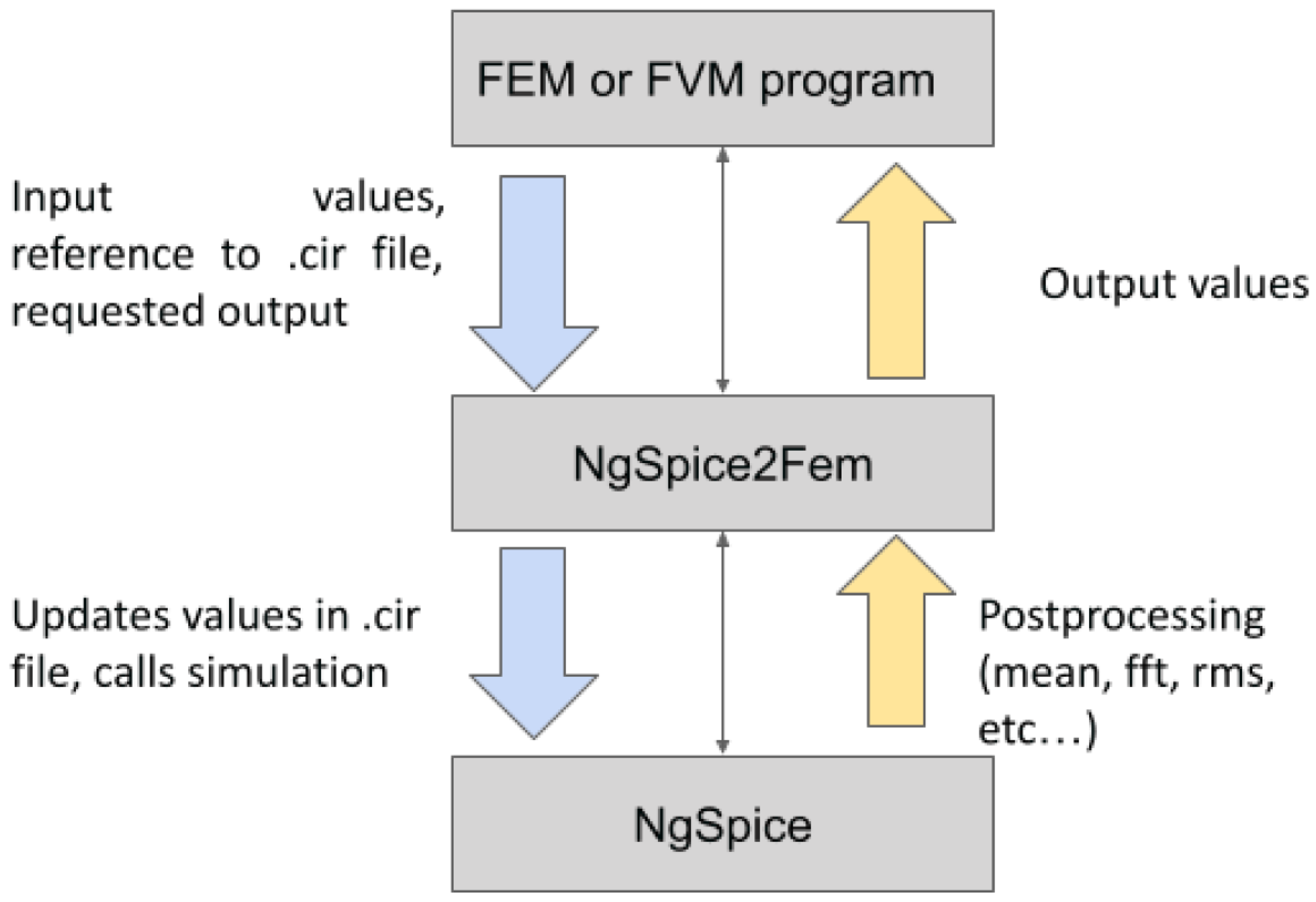

Fig. 1. *Schematic of NgSpice2Fem workflow.*

NgSpice2FEM. Finite element models allow calculating local field values and also global variables like inductance, resistance, power loss, etc. for complicated geometries, but cannot tackle complex electrical circuits. To tackle this problem, small library (500 lines of code) is written to allow coupling of NgSpice with fem package. Library is available in git https://gitlab.com/vadims.geza/ngspice2fem. In this case FEM package is a controller, which calls circuit calculation at needed point. In this work flow NgSpice can be called multiple times during an iterative process. NgSpice calculations are run in the time domain, therefore NgSpice2Fem performs required operations to obtain results that are applicable for the FEM model.

Section 2

Example of work. Crucible filled with aluminum which is molten by means of Joule heating. System consists of a crucible with height 570mm and diameter 316mm filled with aluminum, and an inductor connected to the power circuit (Figure 2). In the described system it is expected that inductance of load changes when aluminum goes over melting temperature. It happens due to increase in aluminum resistivity which leads to increased inductance. Inductance changes are related to variation of skin-depth and magnetic flux area. This, however, leads to changes in operating frequency.

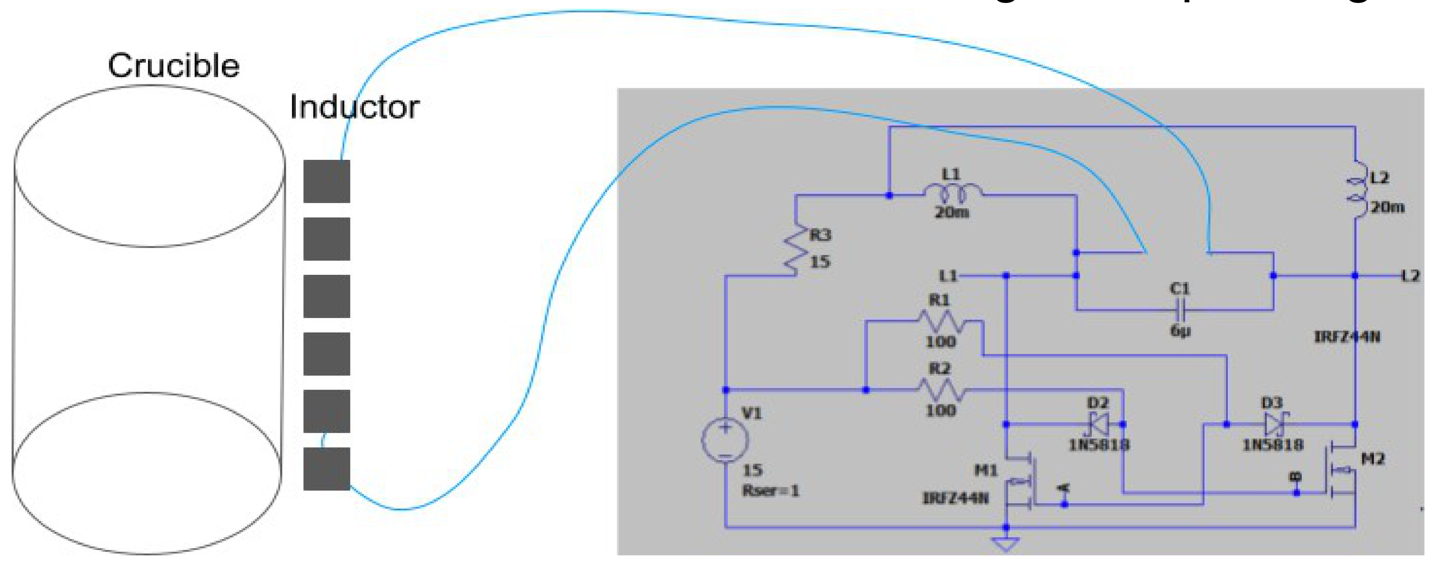

Fig. 2. *FEM model of aluminum melting crucible connected to spice-circuit*

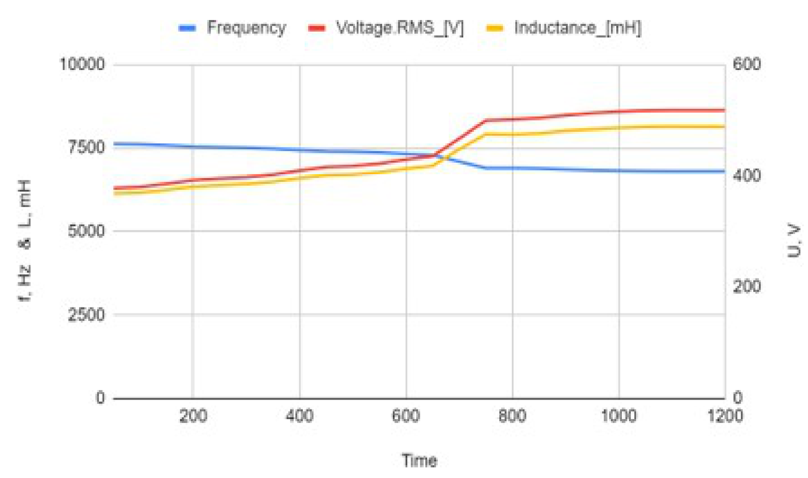

Fig. 3. *Process parameters during aluminum melting*

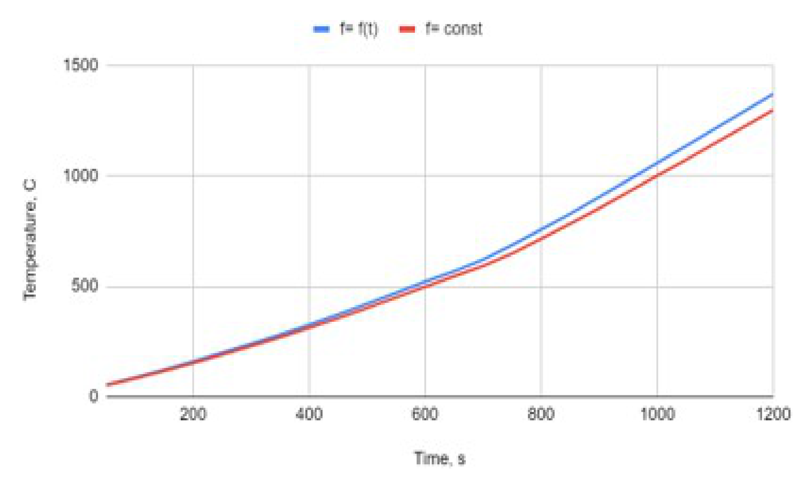

Fig. 4. *Maximal temperature reached in aluminum during heating with fixed and varying frequencies*

In Figure 3 process parameters are shown (Frequency, Voltage, Load Inductance). At the initial stage, frequency is 7550 and it immediately starts to decrease and drops to around 6 kHz at the end of process. Changes in maximal temperature reached in aluminum are shown in Fig. 4 Resulting changes in temperature due to inclusion of frequency variation are approx. 50 degrees. A conclusion can be drawn that taking into account frequency variation can really change the results but these changes are of low impact.

References

[1] T. Quarles . Spice3 version 3f3 user's manual, 1993.
[2] V. Volodin (2008). Modeling of complex electromagnetic component of the spice simulator lt-spice/swcad III. Komponenty i tekhnologii, vol. 4, pp. 175–182.

Conclusions

NgSpice2Fem is a self made library which simplifies calling of Spice circuit simulator an obtaining data required for FEM calculation. The API is still tested with only few applications and software packages. However, it can be freely modified if necessary as it is open source.

A First-Principle Metric For Liquid Metal Capillary Porous Systems

RENAISSANCE FUSION

Simone Mingozzi[a,b], Matteo Iafrati[c]
[a] Renaissance Fusion, France & [b] Tu-Eindhoven, The Netherlands
[c] ENEA Frascati Research Center

TU/e
s.mingozzi@tue.nl
simone.mingozzi@renfusion.eu

1. Overview

- **Liquid Metal (LM) walls** → More compact fusion reactors !? [1].
  - Intrinsic **self-healing** and self-protecting features
- **Capillary Porous systems (CPS)** → Advanced concept for Plasma Facing Components (PFCs)
  - but their **TRL** is low [2].
- In this work, the introduction of a Metric for CPS capillary performance is accomplished via:
  1. **Concept Development: "H-Metric"**
  2. **Numerical Modelling and Simulations**
  3. **Laboratory Experiments**
- A qualitatively good agreement between preliminary simulations and experiments is reached.

2. Motivations and Background

- ***CPS Self-Healing*** → LM must be continuously replenished on the surface
- ***Modelling Gap*** → CPS free-surface flows.
- ***Design Lack*** → A metric for evaluating capillary performance and comparing CPS design is missing.
- **Capillary Pressure is KEY!**
  - **LM replenishment**
  - LM Confinement
- A **metric** idea stems from the physics basis behind **capillary rise in a narrow tube:**

$$\Delta p\Big|_{interface} = p_A - p_0 = -\frac{2\sigma\cos\theta}{\rho g R} \qquad H = \frac{2\sigma\cos\theta}{\rho g R}$$

$$\textit{For CPS,} \qquad \Delta p\Big|_{interface} = f(microstructure)$$

The Height H is a measure for the capillary pressure; hence, it is a metric for capillary performance!

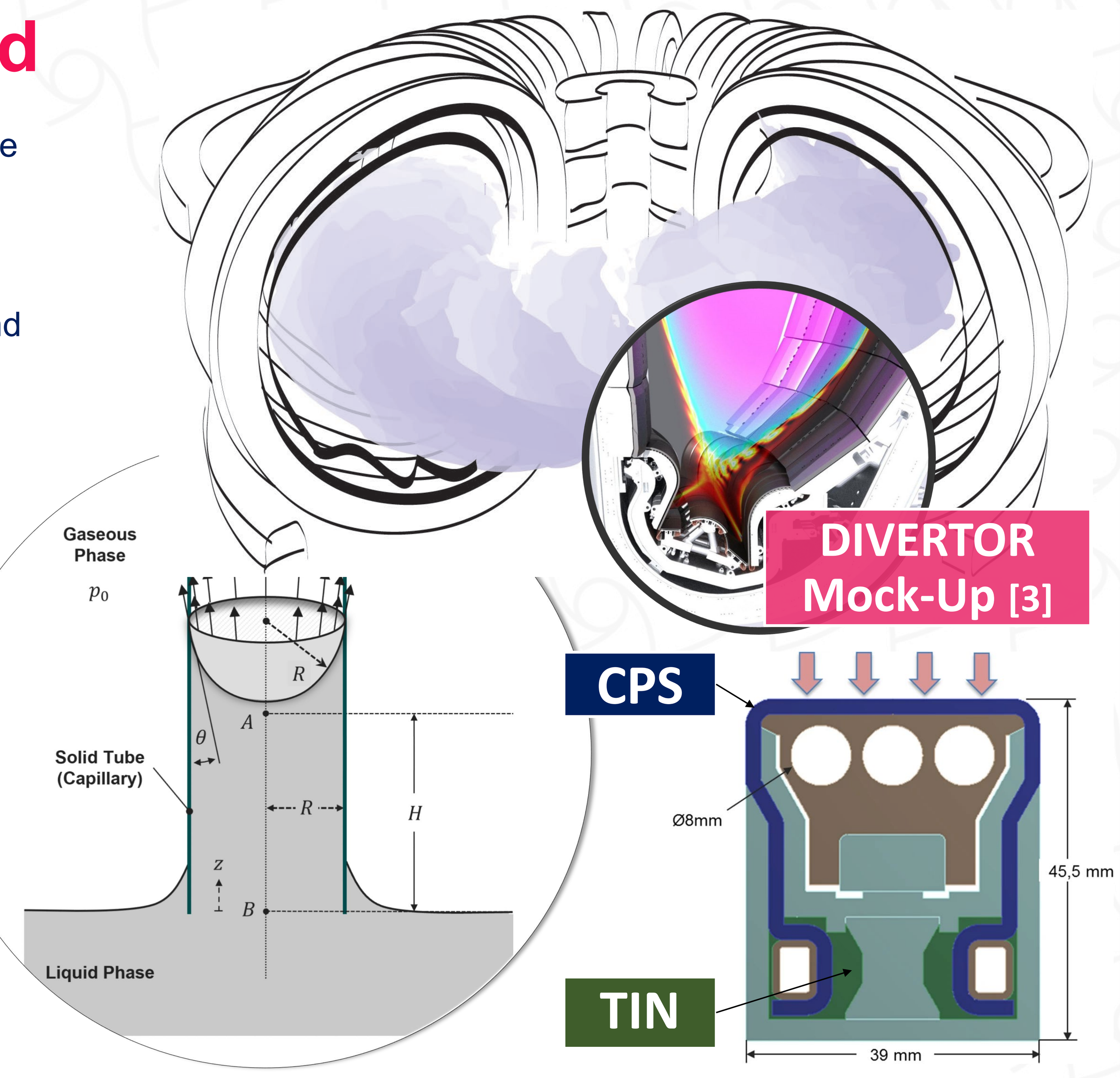

3. Methods

1. Analytical Model:

Modified Lucas-Washburn (MLW) Equation [4]

- Evolutionary Eq. for $h(t)$ in porous medium
- Gravity ✓ , Inertia ✗

$$h(t) = \frac{a}{b}\left(1 + W\left(-e^{-1-\frac{b^2 t}{a}}\right)\right), \text{ with } a = \frac{2\sigma\cos\theta}{por\cdot\mu}\frac{K}{R_{eff}};\ b = \frac{\rho K g}{por\cdot\mu}.$$

2. Experimental Setup:

Industrial 'Oven' with electric Heater

- Vertical CPS samples
- Liquid Tin bath at constant T

3. Geometric Model:

- Fundamental unit: 'Kelvin' Cell
- Spatially Repeated → CPS
- 4 parameters for geometry control

Parametric CAD Model of a uniform CPS

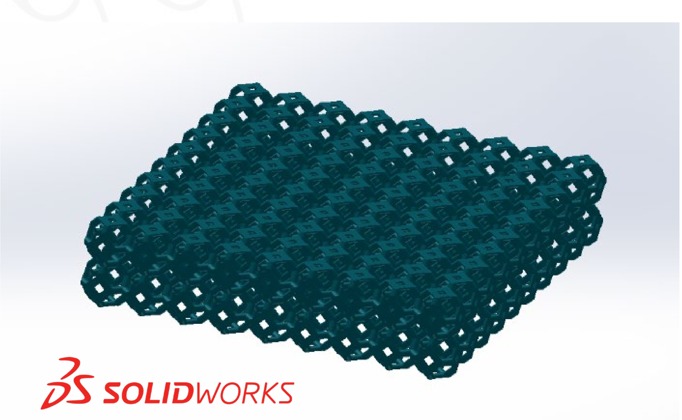

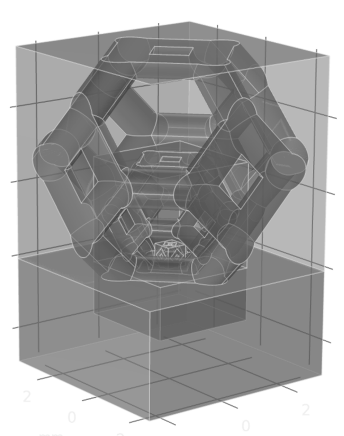

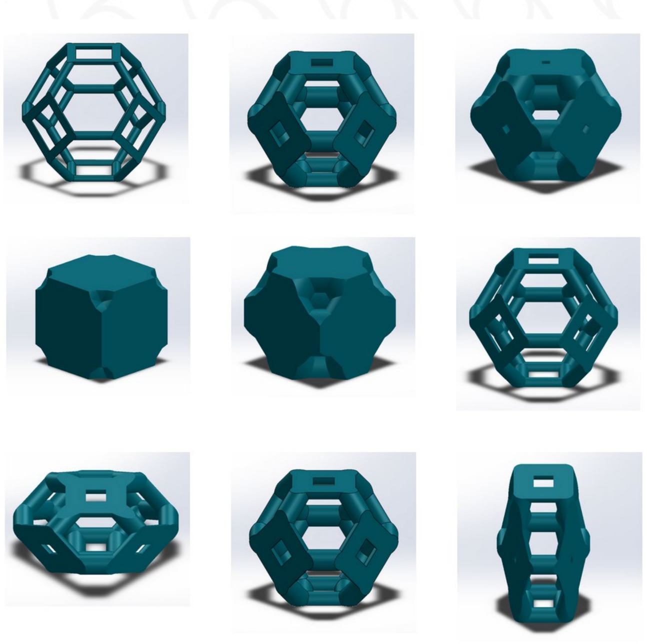

Model Parameters

1. Scaling Factor s
2. Ligament Radius R
3. Ligament Length L
4. Anisotropy

$$A = \frac{h_1}{h_2} = \frac{\textit{Cell Height}}{\textit{Cell Width}}$$

4. Numerical Model

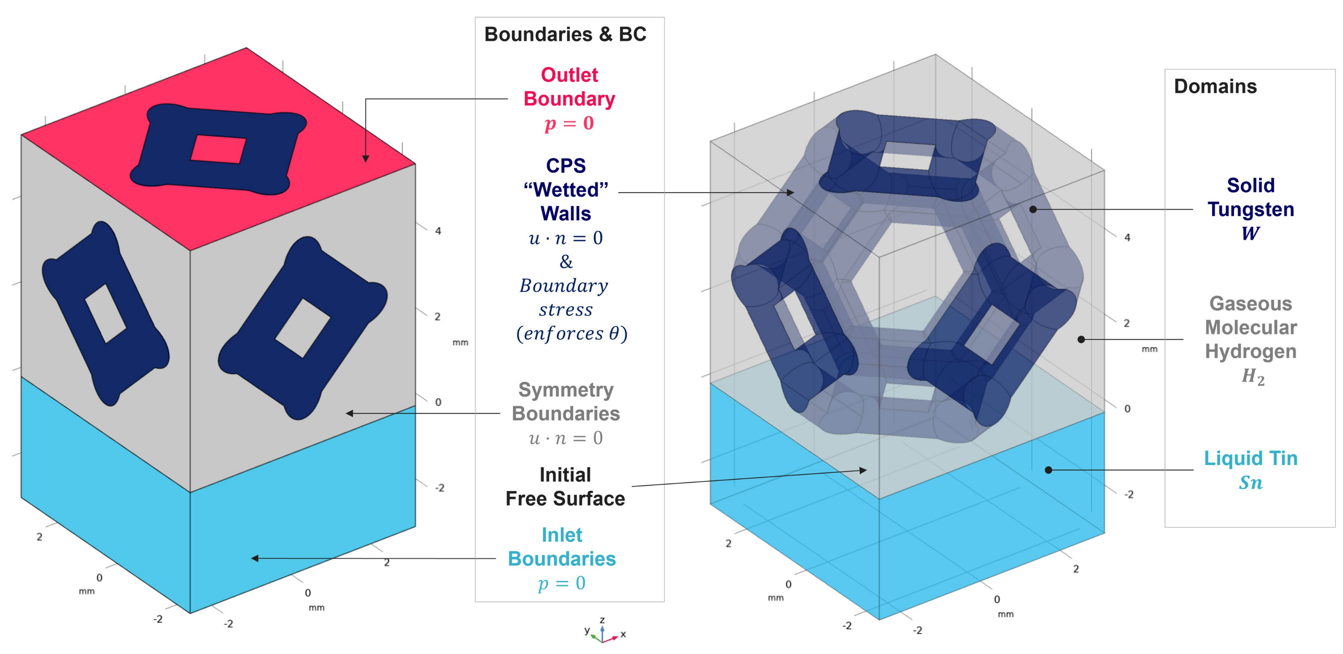

Two-Phase Flow: **Conservative Level-Set (LS) Method [5]**

1. LS Function ϕ governs the interface ($\phi = 0.5$)
2. Navier-Stokes Eqs. coupled with an Evolution equation – advecting the interface

$$\rho\frac{\partial \mathbf{u}}{\partial t} + \rho(\mathbf{u}\cdot\nabla)\mathbf{u} = \nabla\cdot[-p\mathbf{I} + \mu(\nabla\mathbf{u} + (\nabla\mathbf{u})^T)] + \mathbf{F}_{st} + \mathbf{F_g}$$

$$\frac{\partial\phi}{\partial t} + \boldsymbol{u}\cdot\nabla\phi = F$$

3. *BC at the 'wetted wall' enforce contact angle*

$\sigma_{Sn}\left[\frac{N}{m}\right]$	$\rho_{Sn}\left[\frac{kg}{m^3}\right]$	$\mu_{Sn}[10^{-3}Pa\cdot s]$	θ	$\rho_{H_2}\left[\frac{kg}{m^3}\right]$	$\mu_{H_2}[10^{-5}Pa\cdot s]$
0.55	6990	1.85	38°	0.045	1.314

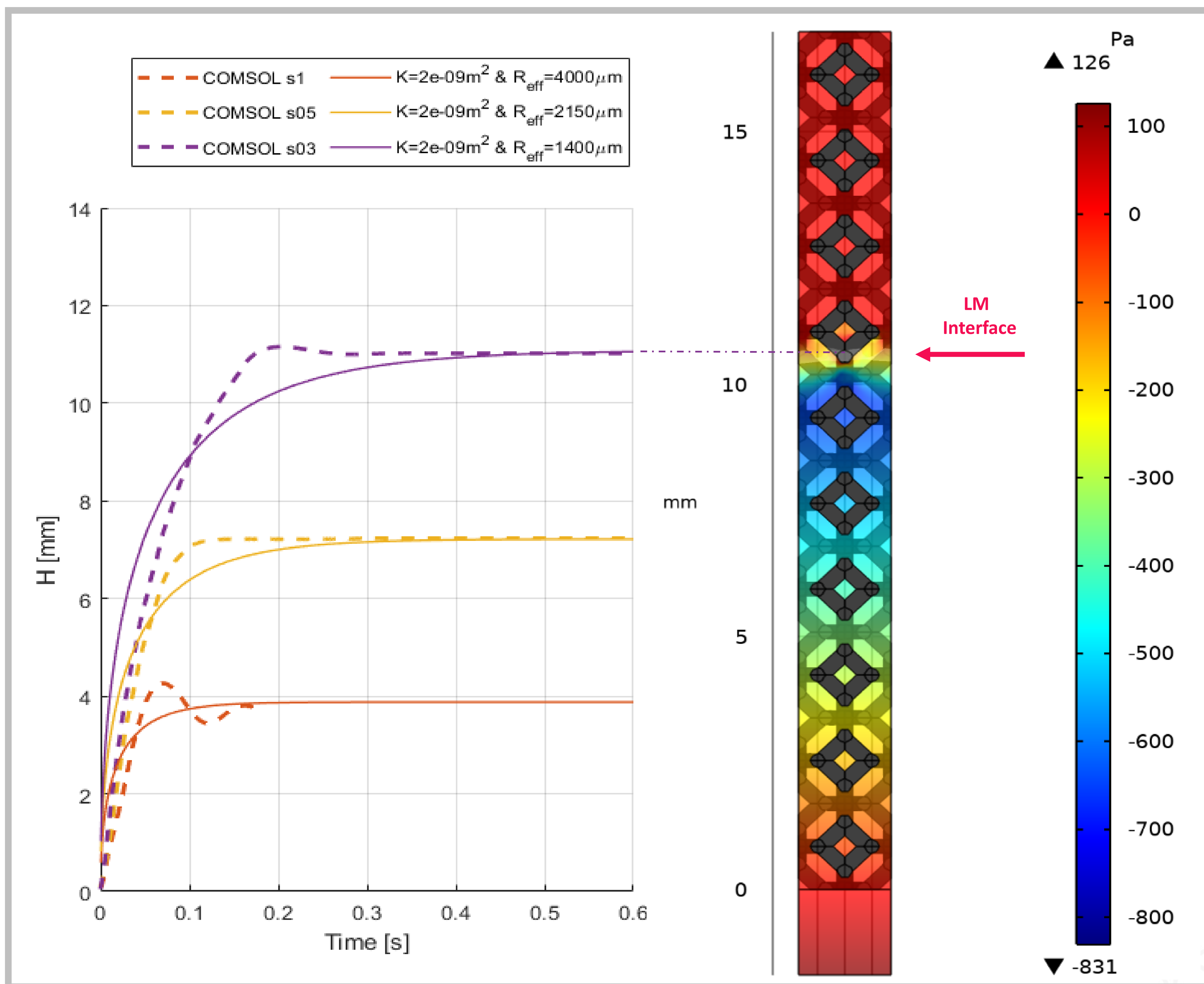

5. Preliminary Numerical Results

Numerical experiments performed with **COMSOL Multiphysics®** show that:

- capillary performance enhancement is possible via geometrical optimization
  - e.g., reducing s the **scaling factor** the capillary height H increases.
- **retro-fitting** of the capillary rise curve using the MLW allows estimation of:
  - **CPS Permeability** K
  - **Effective Radius** R_{eff}
- **capillary pressure** as $f(CPS\ microstructure)$ can be **directly numerically assessed.**

6. Preliminary Experimental Results

- Preliminary experiments
  - show different H for different CPS.
  - qualitatively agree with numerical results (the measured H values).
  ($H \sim cm\ range$ for CPS with pore size in the $mm\ range$)
- ENEA In-house samples were fully wetted → Capillary rise exceeded the maximum heater height.
- Results qualitatively agree with numerical predictions!

Conclusions

- The H-metric provides a valuable design tool to compare different CPS designs **before** testing in fusion devices.
- The developed numerical model could serve as a valuable design tool in predicting and/or optimizing CPS and their capillary flow.

[1] Abdou, M. A. et al. (2001). *On the exploration of innovative concepts for fusion chamber technology.*
[2] R.E. Nygren, F.L. Tabarés (2016). *Liquid surfaces for fusion plasma facing components—A critical review. Part I: Physics and PSI.*
[3] Roccella et al. (2020). *CPS Based Liquid Metal Divertor Target for EU-DEMO.*
[4] Fries N., Dreyer, M. (2008). *An analytic solution of capillary rise restrained by gravity.*
[5] E. Olsson, G. Kreiss (2005). *A conservative level set method for two phase flow.*

https://renfusion.eu